PCCP

ROYAL SOCIETY OF CHEMISTRY

PAPER

View Article Online
View Journal | View Issue

Check for updates

Cite this: *Phys. Chem. Chem. Phys.*, 2025, **27**, 3384

Received 8th December 2024,
Accepted 15th January 2025

DOI: 10.1039/d4cp04624b

rsc.li/pccp

Universal kinetic description for the thermal dehydration of sodium carbonate monohydrate powder across different temperatures and water vapor pressures†

Shunsuke Fukunaga, Yuto Zushi, Mito Hotta and Nobuyoshi Koga*

The thermal dehydration of sodium carbonate monohydrate (SC-MH) exhibits kinetic characteristics that are typical of the thermal decomposition of solids with a reversible nature. One of the characteristics is the physico-geometrical constraints of the reaction due to the heterogeneous reaction feature. Another factor is the considerable impact of the atmospheric and self-generated water vapor on the kinetics. The objective of this study is to develop a universal kinetic description of the dehydration kinetics as a function of temperature, degree of reaction, and partial pressure of water vapor ($p(H_2O)$), deriving kinetic parameters with physico-chemical significance based on the physico-geometrical kinetic model. The kinetic curves for the thermal dehydration of SC-MH were meticulously documented under isothermal and linear nonisothermal conditions at varying $p(H_2O)$ values using humidity-controlled thermogravimetry. The mass loss curves at a constant temperature exhibited a sigmoidal shape following an induction period, irrespective of the $p(H_2O)$ value. As the $p(H_2O)$ value increased, a systematic decrease in the reaction rate was observed. The challenge of providing a kinetic description for the complex reaction process was addressed by a step-by-step approach, which included the following four steps: (1) the development of a universal kinetic description that could be applied across varying temperatures and $p(H_2O)$ values, (2) the incorporation of the effect of self-generated water vapor into the universal kinetic description, (3) the interpretation of the physico-chemical meanings of the apparent kinetic parameters within the universal kinetic description, and (4) the extension of the universal kinetic description to encompass the physico-geometrical kinetic modeling.

1. Introduction

The thermal decomposition of solids with a reversible nature has a range of potential applications in practical processes. These applications include numerous technologies that address energy and environmental issues, including chemical heat storage,[1–6] hydrogen storage,[7–11] capture of various environmentally toxic gases,[12–16] and others. In order to develop and refine these future technologies, it is essential to have a fundamental understanding of both the forward reaction of the thermal decomposition of the candidate compound and its reverse reaction of the solid–gas reaction. In particular, an understanding of the reaction thermodynamics and kinetics is crucial for the design of an effective reaction system for the practical applications. The kinetics of both the thermal decomposition of solids and the solid–gas reaction have been the subject of study for over a century. Consequently, the fundamental kinetic theories and analytical procedures for these reaction processes have been established.[17–21] However, both the reaction processes exhibit intrinsic physico-chemical and physico-geometrical characteristics due to the geometric constraints inherent to the reaction.[22,23] In addition, for reversible reactions occurring in a solid–gas system, both the forward and reverse reactions are significantly affected by the partial pressure of the gaseous species in the system. Therefore, an extension of the fundamental kinetic theories of both forward and reverse reactions is required to describe the kinetics universally as a function of temperature, degree of reaction, and partial pressure of the gaseous species. If possible, the establishment

---

Department of Science Education, Graduate School of Humanities and Social Sciences, Hiroshima University, 1-1-1 Kagamiyama, Higashi-Hiroshima 739-8524, Japan. E-mail: nkoga@hiroshima-u.ac.jp; Fax: +81-82-424-7092; Tel: +81-82-424-7092

† Electronic supplementary information (ESI) available: (S1) Instrumental setup (Fig. S1 and Table S1); (S2) sample characterization (Fig. S2–S4 and Table S2); (S3) thermal behavior in a stream of dry N_2 (Fig. S5–S8); (S4) conventional kinetic analysis (Tables S3, S4 and Fig. S9–S11); (S5) formulation of accommodation function (Fig. S12 and Tables S5, S6); (S6) extended kinetic analysis considering the effect of water vapor (Fig. S13); (S7) effect of water vapor on the individual physico-geometrical reaction steps (Fig. S14, S15 and Tables S7–S9). See DOI: **https://doi.org/10.1039/d4cp04624b**

of a unified kinetic theory that is applicable to both the thermal decomposition of solids and the solid–gas reaction in a solid–gas system is desired to provide the necessary insight into the kinetics of both the reactions in a reversible system and to have a kinetic tool to evaluate the system for possible application.

A universal kinetic description for the thermal decomposition of solids with a reversible nature has recently been achieved by introducing an accommodation function (AF) into the fundamental kinetic equation.[24–38] The AF describes the variation of the reaction rate as a function of the partial pressure of the gaseous species in the reaction system. The practical applicability of the extended kinetic approach has been demonstrated by means of the thermal decomposition of inorganic hydrates,[27,28,33,34,37] carbonates,[29–32,36] and hydroxides[24–26,31,35] over a range of temperatures and partial pressures of the gaseous species. Moreover, the impact of both the external gases in the reaction atmosphere, which serves as the measuring condition for the process, and the self-generated gas from the reaction were taken into account in the universal kinetic approach.[32,36–38] Furthermore, it was demonstrated that the apparent kinetic parameters obtained through the universal kinetic approach can be correlated with the intrinsic kinetic parameters for the reaction by considering the contribution of the thermodynamic parameters of the reaction.[37,38] Moreover, we have achieved the universal description of the kinetics of solid–gas reactions across different temperatures and partial pressures of gaseous species based on the counterpart theory for the thermal decomposition of solids.[39] The practical kinetic analysis was demonstrated for the hydration of lithium sulfate anhydride to form its monohydrate. Consequently, the current objective is to establish a unified theory of the universal kinetic description that is applicable to the thermal decomposition of solids and the solid–gas reaction in a solid–gas system, as well as to develop the practical kinetic procedures for the universal kinetic approach.

The reactions occurring in the sodium carbonate–water vapor system, which include the thermal dehydration of sodium carbonate monohydrate (SC-MH) to form its anhydride (SC-AH) and the hydration reaction of SC-AH with water vapor to form SC-MH, were selected as a model system. The objective was to investigate the parallel applicability of a unified kinetic theory for the universal description of the thermal decomposition of solids and the solid–gas reaction in a specific solid–gas system at different temperatures and partial pressures of the gas involved in the system, as well as to evaluate the merit of the parallel application of a unified theory to the forward and reverse reactions. It was reported that the thermal dehydration of commercially available SC-MH compacted composite grains, consisting of columnar crystals and a matrix produced by the efflorescence of the decahydrate, was found to occur as the partially overlapping two-step process in a stream of dry N_2.[40] The first mass loss step of the thermal dehydration of the SC-MH matrix occurred as a physico-geometrical consecutive process that was composed of the surface reaction (SR) and three-dimensional (3D) phase boundary-controlled reaction (PBR), occurring after the induction period (IP). The second mass loss step was also regulated by the 3D PBR along with the cubic shape of the original SC-MH grain; however, an initial acceleration of the reaction was observed in the reaction stage characterized by overlapping with the previous mass loss step due to the gradual decrease of the self-generated water vapor. Besides, Baglie and DeVore reported a smooth single-step mass loss process for the thermal dehydration of SC-MH powders obtained by efflorescence of the decahydrate in a stream of dry N_2.[41] They suggested a significant dependence of the experimental thermoanalytical curves and the kinetic results on the sample mass (m_0) due to the effect of the self-generated water vapor during the reaction. We have reported the effect of atmospheric water vapor on the thermal dehydration of the SC-MH compacted composite grain.[34] The presence of the atmospheric water vapor resulted in a retardation of both reaction steps in the two-step thermal dehydration process. The kinetics of the individual reaction steps were universally described over different temperatures and the partial pressures of the atmospheric water vapor ($p(H_2O)_{ATM}$). It was proposed that both $p(H_2O)_{ATM}$ and the partial pressure of the self-generated water vapor ($p(H_2O)_{SG}$) be considered for the interpretation of the kinetic behavior of the component reaction steps in the scheme of the universal kinetic description. The reversible nature of the thermal dehydration of SC-MH and the subsequent hydration of SC-AH at a lower temperature in the presence of water vapor has been reported by Ball *et al.*[42] The preliminary experiments conducted for this study using a humidity-controlled thermogravimetry (TG) system yielded evidence confirming a smooth single-step mass gain process following an IP at a constant temperature for the SC-AH produced by the thermal dehydration when exposed to a stream of wet N_2 with a controlled $p(H_2O)_{ATM}$ value. Furthermore, a trend of the promotion of the hydration reaction rate was observed with decreasing temperature and increasing $p(H_2O)_{ATM}$. Therefore, both the thermal dehydration of SC-MH powder and the hydration of SC-AH were found to exhibit specific physico-geometrical reaction behaviors and are significantly influenced by the water vapor present in the reaction system, while the overall reactions are characterized by smooth single-step mass change processes with a reversible nature. The observed behaviors of the reactions in the sodium carbonate–water vapor system indicate its suitability as a model system for the study of the parallel kinetic approaches to both the forward and reverse reactions using a unified theory for the universal kinetic description.

This article presents the initial findings of a series of kinetic studies on the reversible reactions in the sodium carbonate–water vapor system. It reports the universal kinetic description of the forward reaction of the thermal dehydration of SC-MH powders over a range of temperatures and $p(H_2O)$ values, including $p(H_2O)_{SG}$ and $p(H_2O)_{ATM}$. The theory and analytical procedures of the universal kinetic description for the thermal decomposition of solids, which were previously established, were refined in stages towards further extension and the establishment of a unified theory applicable to both the forward and reverse reactions. Following an examination of the results of the conventional kinetic analysis applied to the thermal dehydration of SC-MH powders at varying $p(\mathrm{H_2O})_{\mathrm{ATM}}$ values, the universal kinetic description of the IP and mass loss processes across diverse temperatures and $p(\mathrm{H_2O})_{\mathrm{ATM}}$ values was attained through the implementation of a formal kinetic analysis, which encompassed the assessment of the isoconversional and isothermal kinetic relationships. Subsequently, the effect of $p(\mathrm{H_2O})_{\mathrm{SG}}$ was incorporated into the extended kinetic equation for extending the universal kinetic approach to include the reactions in a stream of dry N_2, *i.e.*, $p(\mathrm{H_2O})_{\mathrm{ATM}} \approx 0$. In addition, the physico-chemical significance of the apparent kinetic parameters determined through the universal kinetic approach was examined in order to obtain a correlation with the intrinsic kinetic parameters. Finally, the universal kinetic approach, founded upon the formal kinetic analysis scheme, was translated into physico-geometrical kinetic modeling for describing the physico-geometrical consecutive IP–SR–PBR process, which is characteristic of the thermal dehydration of SC-MH powders. The results obtained at each analytical stage are expected to provide further insight into the kinetics of the thermal dehydration of SC-MH and the thermal decomposition of solids in general. Furthermore, the strategy proposed for the universal kinetic approach to the thermal dehydration of SC-MH will be extended to the reverse reaction of the hydration of SC-AH, which will be reported separately as the counterpart of this article.

2. Experimental

2.1 Sample and its characterization

The SC-MH powders were prepared by the efflorescence of the chemical reagent of its decahydrate ($\mathrm{Na_2CO_3{\cdot}10H_2O}$; special grade, FUJIFILM Wako Chem.) by exposure at an ambient temperature of 298 K and flowing dry N_2 at a flow rate (q_v) of 100 $\mathrm{cm^3\ min^{-1}}$ in a tube furnace overnight. The solid product obtained by the efflorescence of $\mathrm{Na_2CO_3{\cdot}10H_2O}$ was characterized by powder X-ray diffractometry (XRD), Fourier transform infrared spectrometry (FTIR), and simultaneous TG–differential thermal analysis (DTA) measurements. The XRD pattern of the efflorescence product pressed onto a sample holder plate was recorded using a diffractometer (RINT 2200V, Rigaku). While irradiating the sample with Cu-K_α (40 kV, 20 mA), the 2θ value was scanned from 5° to 60° in 0.02° steps at a scanning speed of 4° $\mathrm{min^{-1}}$ to record the XRD pattern. The FTIR spectrum was recorded using a spectrometer (FT-IR 8400S, Shimadzu) with the diffuse reflection method. After the sample was diluted with KBr, the FTIR measurement was performed in the wavenumber range of 4600–400 $\mathrm{cm^{-1}}$ with a resolution of 4 $\mathrm{cm^{-1}}$, and the spectra were accumulated 40 times. The sample was subjected to TG–DTA measurements to determine the mass loss value during thermal dehydration and to investigate the changes in reaction behavior as a function of m_0 and q_v of purge gas (*i.e.*, dry N_2). For the sample weighed in a Pt pan (diameter: 6 mm; depth: 2.5 mm), TG–DTA measurements were performed using a top-loading type instrument (DTG-60, Shimadzu) under isothermal conditions at a temperature of 315 K and under linear nonisothermal conditions at a heating rate (β) of 3 K $\mathrm{min^{-1}}$ in a stream of dry N_2, for which m_0 and q_v were varied in the ranges of 2–13 mg and 10–100 $\mathrm{cm^3\ min^{-1}}$, respectively.

The morphology of the efflorescence product was characterized by microscopic observations using a scanning electron microscope (SEM) and measurement of the Brunauer–Emmett–Teller (BET) specific surface area (S_{BET}). The SEM observations were performed using an instrument (JSM-6510, JEOL) in the reflection mode after the sample particles were thinly coated with a Pt layer by sputtering (JEC-1600, JEOL; 30 mA, 30 s). The S_{BET} value was determined by the BET single point method using an instrument (FlowSorb II, Micromeritics).

2.2 Tracking of the thermal dehydration in a stream of dry N_2

The thermal dehydration of SC-MH in an inert gas atmosphere of a stream of dry N_2 (q_v = 300 $\mathrm{cm^3\ min^{-1}}$) was systematically tracked using a horizontal TG–DTA instrument (TG-8121, Thermoplus Evo2 system, Rigaku), for which the m_0 weighed into a Pt pan (diameter: 5 mm; depth: 2.5 mm) was controlled to be 5.00 ± 0.05 mg. TG–derivative TG (DTG) curves were recorded in both isothermal and linear nonisothermal modes. In the isothermal mode, the TG–DTG measurements were conducted by initially heating the sample from 303 K to a preset temperature ($312 \leq T/\mathrm{K} \leq 332$) at a β of 5 K $\mathrm{min^{-1}}$, and subsequently maintaining the temperature until the mass loss process was completed. In the linear nonisothermal mode, the sample was heated linearly from 303 to 423 K at various β values of 0.5–10 K $\mathrm{min^{-1}}$ to record TG–DTG curves. In particular, it was confirmed prior to the TG–DTG measurements that the N_2 flow rate above 300 $\mathrm{cm^3\ min^{-1}}$ does not cause any significant change in the results compared to those at 300 $\mathrm{cm^3\ min^{-1}}$.

Changes in the sample particle morphologies in the course of the thermal dehydration were investigated using SEM. The samples (m_0 = 5.00 ± 0.05 mg) were partially dehydrated to varying degrees of reaction (α) using a TG–DTA instrument (DTG-60) by heating them in isothermal mode at T = 313 K for different times in a stream of dry N_2 (q_v = 100 $\mathrm{cm^3\ min^{-1}}$). The samples retained from the TG–DTA instrument were coated with a thin Pt layer *via* sputtering and subsequently examined under a SEM (JSM-6510).

2.3 Tracking of the thermal dehydration in a stream of wet N_2

TG–DTA measurements were systematically conducted for the thermal dehydration of SC-MH in the presence of water vapor using a TG–DTA system (TG-8120, Thermoplus 2, Rigaku) equipped with a humidity controller (HUM-1, Rigaku) in a stream of wet N_2 (q_v = 400 $\mathrm{cm^3\ min^{-1}}$) with various $p(\mathrm{H_2O})_{\mathrm{ATM}}$ values, for which the identical sampling procedures, including the sample pan and m_0 values, were employed as in the measurements in a stream of dry N_2.

A series of TG–DTG curves were recorded by heating the sample to 393 K under linear nonisothermal conditions at a fixed β of 5 K $\mathrm{min^{-1}}$ in a stream of wet N_2 characterized by different $p(\mathrm{H_2O})_{\mathrm{ATM}}$ values ($0.2 \leq p(\mathrm{H_2O})_{\mathrm{ATM}}/\mathrm{kPa} \leq 12.8$). Moreover, by selecting three $p(\mathrm{H_2O})_{\mathrm{ATM}}$ values of 0.4, 3.7, and

9.2 kPa, the TG–DTG curves were systematically recorded in both isothermal and linear nonisothermal modes, in a manner analogous to the measurements conducted in a stream of dry N_2. In the isothermal modes, the preset isothermal temperature ranges were in the range of 324–336 K, 337–348 K, and 352–362 K for the measurements conducted in a stream of wet N_2 with $p(H_2O)_{ATM}$ values of 0.4, 3.6, and 8.9 kPa, respectively. The measurements in the linear nonisothermal mode were conducted at varying β values, ranging from 0.5 to 10 K min^{-1}.

The calibrations of the TG–DTA instruments (DTG-60, TG-8121, and TG-8120; Table S1, ESI†) and the instrumental controls for the TG–DTG measurements in a stream of wet N_2 (Fig. S1, ESI†) are described in the ESI† (Section S1).

3. Results and discussion

3.1 Sample characterization

The sample exhibited an XRD pattern identical to that previously reported for SC-MH (orthorhombic, S.G. = $P2_1ab(29)$, a = 6.4720, b = 10.7240, c = 5.2590, $\alpha = \beta = \gamma$ = 90.000, ICDD-PDF 01-070-0845, Fig. S2, ESI†).[43] The FTIR spectrum of the sample exhibited absorption peaks attributed to H_2O and CO_3^{2-} (Fig. S3, ESI†).[44] The assignment of individual absorption peaks is listed in Table S2 (ESI†). The sample was identified as an agglomerate of rounded particles with a diameter of several μm (Fig. S4, ESI†), exhibiting a S_{BET} value of 1.23 ± 0.06 $m^2 g^{-1}$.

3.2 Thermal behavior in a stream of dry N_2

Fig. S5 (ESI†) illustrates the impact of m_0 on the TG–DTG–DTA curves for the thermal dehydration of SC-MH under isothermal and linear nonisothermal conditions in a stream of dry N_2. Similarly, the influence of q_v on the TG–DTG–DTA curves is shown in Fig. S6 (ESI†). The thermoanalytical (TA) curves exhibited a consistent pattern of mass loss, accompanied by an endothermic effect, regardless of the measurement conditions. The mass loss value was determined to be 14.83 ± 0.59%, which corresponds to the calculated value for the thermal dehydration of SC-MH to form its anhydride (SC-AH) (Δm = 14.53%) as follows.

$$\mathrm{Na_2CO_3 \cdot H_2O(s) \rightarrow Na_2CO_3(s) + H_2O(g)} \\ (\Delta_r H^\circ_{298} = 58.6\ \mathrm{kJ\ mol^{-1}},\ \Delta_r S^\circ_{298} = 155.4\ \mathrm{J(mol\ K)^{-1}}), \tag{1}$$

where the thermodynamic parameters of the reaction were calculated using the literature values for $Na_2CO_3{\cdot}H_2O(s)$, $Na_2CO_3(s)$, and $H_2O(g)$.[45] Under isothermal conditions (T = 315 K), the IP was observed prior to the initiation of the mass loss process (Fig. S5(a) and S6(a), ESI†). Notably, the duration of IP (t_{IP}) remained constant at a constant temperature, irrespective of m_0 (Fig. S5(a), ESI†). Conversely, it was observed that t_{IP} was shortened with increasing q_v (Fig. S6(a), ESI†). The mass loss curves displayed a sigmoidal shape under isothermal conditions. The reaction time for the mass loss process was observed to increase with increasing m_0 (Fig. S5(a), ESI†), whereas it was observed to decrease with an increase in the q_v value. The corresponding behaviors of the TA curves were also observed under linear nonisothermal conditions (β = 3 K min^{-1}), exhibiting a systematic shift of the reaction temperature to higher temperatures with increasing m_0 (Fig. S5(b), ESI†) and to the lower temperatures with increasing q_v (Fig. S6(b), ESI†). The retardation of the mass loss process with the increase in m_0 has been previously reported by Baglie and DeVore.[41] They proposed an explanation for this phenomenon based on the effect of self-generated water vapor on the kinetics. It should also be noted that, as m_0 varies, the thickness of the sample bed in the pan changes systematically, resulting in a change in the reaction geometry.[46–49] Therefore, it is generally recommended to use as small a m_0 as possible when collecting kinetic data using TA.[50] Similarly, the variation in the TA curves with q_v may be interpreted in a manner analogous to that described above. With increasing q_v, the removal effectiveness of the evolved water vapor from the reaction system increases, thereby reducing the effect of self-generated water vapor on the kinetics.

Fig. S7 and S8 (ESI†) illustrate the alterations in the XRD pattern of the sample throughout the heating process under stepwise isothermal and isothermal conditions, respectively. The transformation of the crystalline phase was observed under stepwise isothermal conditions in a temperature range between 333 and 353 K (Fig. S7(a), ESI†), which corresponds to the temperature range of mass loss observed in TG. The solid product was identified as SC-AH (monoclinic, $C2/m(12)$, a = 8.9040, b = 5.2390, c = 6.0420, α = 90.000, β = 101.350, γ = 90.000, ICDD PDF 05-001-0022; Fig. S7(b), ESI†).[51] Under isothermal conditions at 333 K, no discernible alteration in the XRD pattern was observed during the initial 60 min, indicating that there was no change in the crystal phase during IP. Subsequently, the XRD peaks attributed to SC-MH exhibited gradual attenuation, whereas those of SC-AH demonstrated gradual growth between 60 and 180 min. Notably, no additional XRD peaks were observed during the thermal dehydration of SC-MH, which resulted in the formation of SC-AH.

3.3 Conventional kinetic analysis

Fig. 1 depicts the TG–DTG curves for the thermal dehydration of SC-MH under isothermal conditions at varying temperatures, recorded under distinct atmospheric conditions in a stream of dry or wet N_2 with three different $p(H_2O)_{ATM}$ values: 0.4, 3.6, and 8.9 kPa. Irrespective of the prevailing atmospheric conditions, an identifiable IP was observed under isothermal conditions. The t_{IP} value was found to increase systematically with a decrease in reaction temperature at each $p(H_2O)_{ATM}$ value. The subsequent mass loss process exhibited a sigmoidal curve, irrespective of the reaction temperature and the atmospheric conditions. Notably, the optimal reaction temperature for TA measurements under isothermal conditions should be increased as the $p(H_2O)_{ATM}$ value is elevated.

From the TG–DTG curves under isothermal conditions, the t_{IP} value was determined based on an empirical definition as the time elapsed between the attainment of the preset isothermal holding temperature (time zero) and the observation of a mass loss of 2.0 μg. When the IP process is not significantly

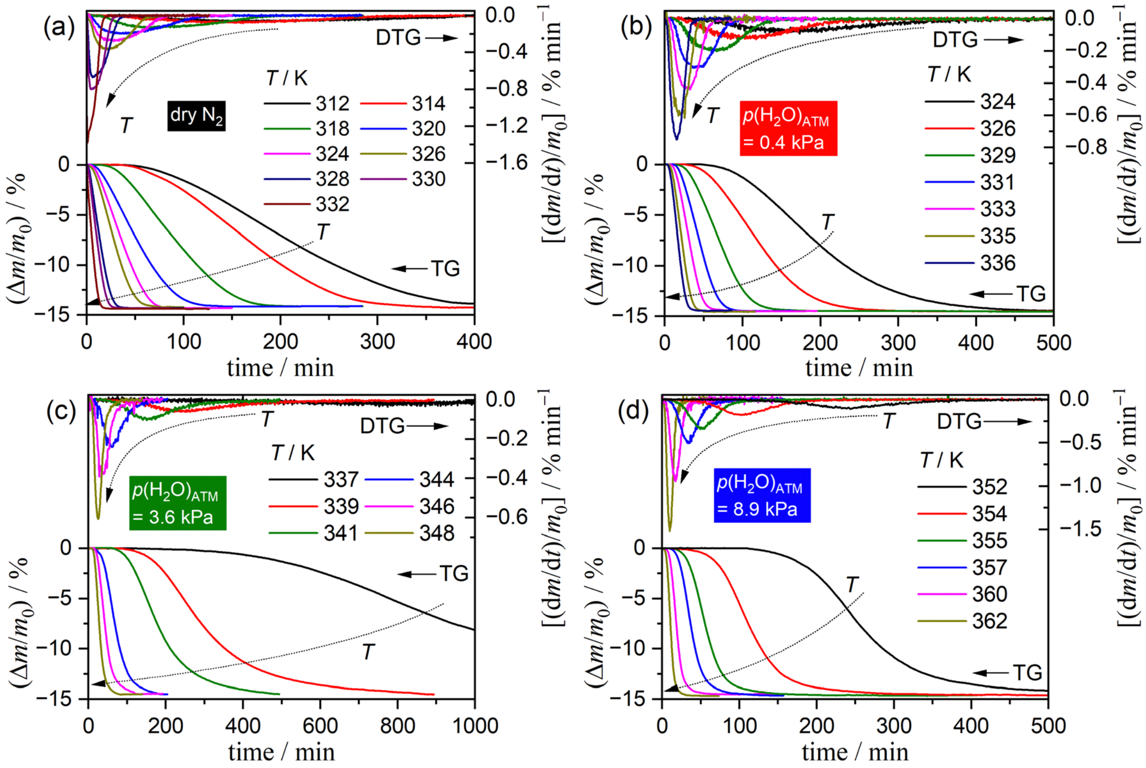

Fig. 1 TG–DTG curves for the thermal dehydration of SC-MH to form SC-AH under isothermal conditions at varying temperatures, recorded under different atmospheric conditions in a stream of dry or wet N_2 with different controlled $p(H_2O)_{ATM}$ values: (a) dry N_2 ($p(H_2O)_{ATM} < 0.2$ kPa; $m_0 = 4.92 \pm 0.14$ mg), (b) wet N_2 ($p(H_2O)_{ATM} = 0.4$ kPa; $m_0 = 5.01 \pm 0.02$ mg), (c) wet N_2 ($p(H_2O)_{ATM} = 3.6$ kPa; $m_0 = 4.98 \pm 0.03$ mg), and (d) wet N_2 ($p(H_2O)_{ATM} = 8.9$ kPa; $m_0 = 5.01 \pm 0.01$ mg). Time zero was defined as the moment at which the sample temperature reached the preset temperature for isothermal measurements.

affected by atmospheric water vapor, the kinetics can be analyzed based on the fundamental kinetic equation:[52–58]

$$\frac{1}{t_{IP}} = A_{IP}\exp\left(-\frac{E_{a,IP}}{RT}\right)f(\alpha_{IP}), \tag{2}$$

where A_{IP} and $E_{a,IP}$ are the apparent Arrhenius preexponential factor and activation energy for the IP, respectively. R is the gas constant. The zero-order kinetic model is employed empirically for the kinetic model function $f(\alpha_{IP})$ with the definition of α_{IP} as the conversion of the IP process. Then, the logarithmic form of eqn (2) can be used to determine the kinetic parameters *via* an Arrhenius-type plot of $\ln(1/t_{IP})$ *versus* reciprocal temperature. Fig. 2 illustrates the results of conventional kinetic analysis for the IP under different atmospheric conditions. The t_{IP} exhibited an exponential increase with decreasing temperature under individual atmospheric conditions (Fig. 2(a)). However, at a selected temperature, an increase in the $p(H_2O)_{ATM}$ value was observed to result in an increase in the t_{IP}. Although the Arrhenius-type plot exhibited a statistically significant linear correlation for the IP process at a fixed $p(H_2O)_{ATM}$ value (Fig. 2(b)), the linear correlation, as characterized by the slope and intercept, varied systematically with the $p(H_2O)_{ATM}$ value. Specifically, there was an increase in both the slope and intercept with increasing $p(H_2O)_{ATM}$ value. Table S3 (ESI†) lists the apparent kinetic parameters for the IP process under individual atmospheric conditions. The results of conventional kinetic analysis can be employed to reproduce the experimental data (Fig. 2(a)). However, the disparate kinetic results for the IP process under different atmospheric conditions indicate the necessity of incorporating a $p(H_2O)_{ATM}$ term into the kinetic equation to achieve a universal kinetic description.

Fig. 3 illustrates the TG–DTG curves recorded under linear nonisothermal conditions at varying β values for the thermal dehydration of SC-MH in a stream of dry or wet N_2 with distinct $p(H_2O)_{ATM}$ values. At a given $p(H_2O)_{ATM}$ value, the TG–DTG curves shifted towards higher temperatures with increasing β. Furthermore, at a selected β, the TG–DTG curves shifted towards higher temperatures with increasing $p(H_2O)_{ATM}$ (Fig. S9, ESI†).

For the kinetic analysis of the mass loss process of the thermal dehydration, individual TG–DTG curves recorded under isothermal (Fig. 1) and linear nonisothermal (Fig. 3) conditions were transformed into kinetic curves by calculating the α value with reference to the total mass loss value. This approach yielded a series of data points (time, T, α, $d\alpha/dt$) representing the kinetic data of individual reactions at varying temperatures and $p(H_2O)_{ATM}$ values. At each $p(H_2O)_{ATM}$ value, the kinetic curves form a specific coordinate surface in the 3D kinetic coordinate of T^{-1}, α, and $\ln(d\alpha/dt)$ (Fig. S10, ESI†). It is notable that distinct coordinate surfaces were obtained for the

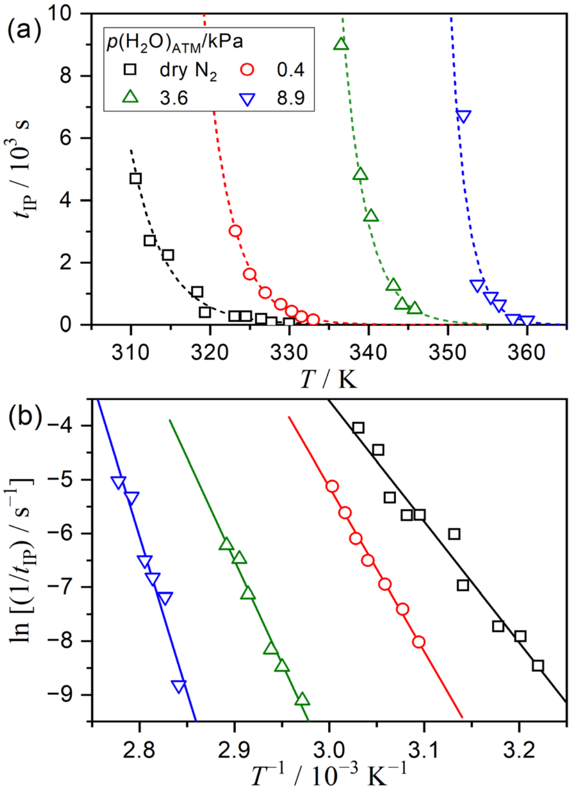

Fig. 2 Results of the conventional kinetic analysis for the IP process of the thermal dehydration of SC-MH under isothermal conditions in a stream of dry or wet N_2 with different $p(H_2O)_{ATM}$ values, conducted using the fundamental kinetic equation (eqn (2)): (a) t_{IP} values at varying temperatures and $p(H_2O)_{ATM}$ values and (b) Arrhenius-type plots for the IP process at individual $p(H_2O)_{ATM}$ values. The dashed lines in (a) represent the replication curve, which was calculated using the results of the Arrhenius-type plots shown in (b).

reactions at varying $p(H_2O)_{ATM}$ values. As a preliminary kinetic approach, the kinetic data at individual $p(H_2O)_{ATM}$ values, including those recorded in a stream of dry N_2, were analyzed separately based on the fundamental kinetic equation, which does not consider the effect of $p(H_2O)_{ATM}$.[59,60]

$$\frac{d\alpha}{dt} = A\exp\left(-\frac{E_a}{RT}\right)f(\alpha), \qquad (3)$$

where A, E_a, R, and $f(\alpha)$ are the Arrhenius preexponential factor, apparent activation energy, gas constant, and kinetic model function, respectively.

The formal kinetic analysis based on eqn (3) was conducted using its logarithmic form.

$$\ln\left(\frac{d\alpha}{dt}\right) = \ln[Af(\alpha)] - \frac{E_a}{RT} \qquad (4)$$

The coordinate surface in the 3D kinetic coordinate at individual $p(H_2O)_{ATM}$ values is characterized by two distinct kinetic relationships: the isoconversional and isothermal relationships. Fig. 4 presents a comparison of the results of the conventional kinetic analysis with regard to the isoconversional and isothermal kinetic relationships for the reactions under different atmospheric conditions. The isoconversional kinetic relationship was investigated *via* $\ln(d\alpha/dt)$ *versus* T^{-1} plots at various α values, which is known as the Friedman plot.[61] Irrespective of $p(H_2O)_{ATM}$ value, the Friedman plots at individual α values exhibited approximately linear correlation (Fig. 4(a)), yet a convex feature of the linearity was observed across all α values (Fig. S11, ESI†). Furthermore, a reduction in the slope of the plot was observed as the reaction proceeded. As the $p(H_2O)_{ATM}$ value increased, the slope was systematically elevated, accompanied by an increase in the curvature of the plot. Consequently, the apparent E_a value initially exhibited a decreasing trend and subsequently reached a constant value at individual $p(H_2O)_{ATM}$ values. In addition, the E_a value at a selected α value demonstrated a systematic increase with raising $p(H_2O)_{ATM}$ value (Fig. 4(b)). Table S4 (ESI†) lists the average E_a value ($0.10 \leq \alpha \leq 0.90$) for the reactions at individual $p(H_2O)_{ATM}$ values. The average E_a value exhibited a systematic increase from 115.5 kJ mol^{-1} in a stream of dry N_2 to 246.9 kJ mol^{-1} in a stream of wet N_2 with $p(H_2O)_{ATM}$ = 9.2 kPa.

The isothermal kinetic relationship of the reactions under individual atmospheric conditions was analyzed by constructing an experimental master plot. The hypothetical reaction rate ($d\alpha/d\theta$) at the infinite temperature was calculated at varying α values according to the following equation,[62–67] utilizing the average E_a value listed in Table S4 (ESI†).

$$\frac{d\alpha}{d\theta} = \left(\frac{d\alpha}{dt}\right)\exp\left(\frac{E_a}{RT}\right) = Af(\alpha)$$
$$\text{with } \theta = \int_0^t \exp\left(-\frac{E_a}{RT}\right)dt, \qquad (5)$$

where the Ozawa's generalized time (θ) represents the hypothetical reaction time at infinite temperature.[62,63] The experimental master plot of $d\alpha/d\theta$ *versus* α exhibited the maximum reaction rate midway through the reaction, irrespective of the atmospheric conditions (Fig. 4(c)). In light of the distinctive characteristics of the thermal decomposition of solids, which is governed by a contracting geometry scheme, the initial acceleration of the reaction rate can be attributed to the SR. Conversely, the subsequent deceleration can be ascribed to the shrinkage of the reaction interface, which advances towards the center of the reacting particles. The reaction at a lower $p(H_2O)_{ATM}$ value displayed a more rapid acceleration, whereas the reaction at a higher $p(H_2O)_{ATM}$ value exhibited a more rapid deceleration. This variation of the experimental master plot was accompanied by a systematic shift of the α value at the maximum reaction rate with increasing $p(H_2O)_{ATM}$ from α = 0.21 in a stream of dry N_2 to α = 0.36 in a stream of wet N_2 with $p(H_2O)_{ATM}$ = 9.2 kPa. The variation of the isothermal kinetic relationship with atmospheric conditions was parameterized using an empirical kinetic model function, known as the Šesták-Berggren model: SB(m, n, p).[68–70]

$$f(\alpha) = \alpha^m(1-\alpha)^n[-\ln(1-\alpha)]^p \qquad (6)$$

According to eqn (5), the most accurate representation of the experimental master plot was achieved by optimizing A and the

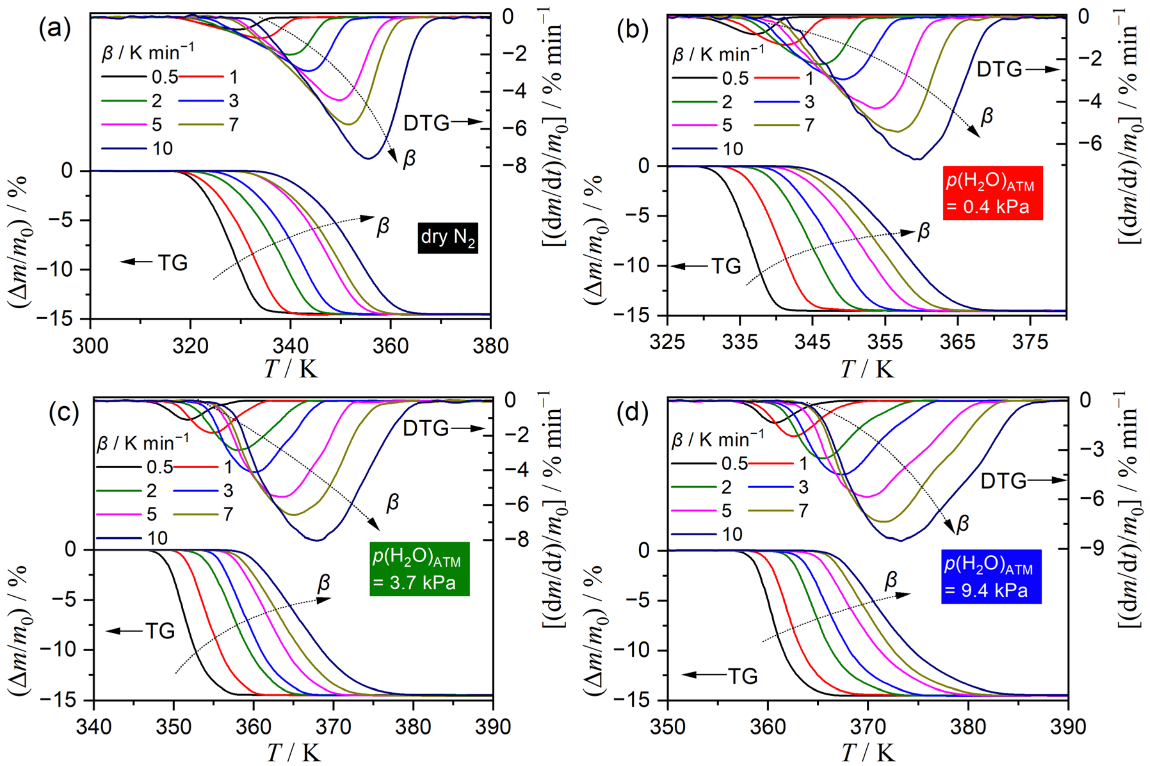

Fig. 3 TG–DTG curves recorded under linear nonisothermal conditions at varying β values for the thermal dehydration of SC-MH in a stream of dry or wet N_2 with different $p(H_2O)_{ATM}$ values: (a) dry N_2 ($p(H_2O)_{ATM}$ < 0.2 kPa; m_0 = 5.01 ± 0.04 mg), (b) wet N_2 ($p(H_2O)_{ATM}$ = 0.4 kPa; m_0 = 5.00 ± 0.04 mg), (c) wet N_2 ($p(H_2O)_{ATM}$ = 3.7 kPa; m_0 = 4.99 ± 0.03 mg), and (d) wet N_2 ($p(H_2O)_{ATM}$ = 9.4 kPa; m_0 = 5.00 ± 0.03 mg).

kinetic exponents in SB(m, n, p) through the application of nonlinear least-squares analysis, as described by the Levenberg–Marquardt algorithm. The optimized kinetic parameters are listed in Table S4 (ESI†). The optimized values of A and the exponent n in SB(m, n, p) exhibited a systematic increase with an increase in the $p(H_2O)_{ATM}$ value. The increase in the A value compensates for the increase in the E_a value, exhibiting a generally observed trend of the kinetic compensation effect, namely, a linear correlation between E_a and $\ln A$: $\ln A = a + bE_a$.[38,71–80] Furthermore, assuming a contracting geometry-type reaction, the deceleration stage of the second half of the reaction was fitted by the PBR model: R(n).[81]

$$f(\alpha) = n(1-\alpha)^{1-1/n}, \qquad (7)$$

where n is the geometrical dimension of the reaction interface shrinkage. The optimized n value demonstrated a tendency to increase with raising $p(H_2O)_{ATM}$ values, specifically from n = 1.82 in a stream of dry N_2 to n = 2.93 at $p(H_2O)_{ATM}$ = 9.2 kPa.

In conclusion, the conventional kinetic analysis, which ignores the effect of atmospheric water vapor, provides an empirical characterization of the kinetic behavior of the reaction under specific atmospheric conditions. However, it does not offer a universal kinetic description that can be applied across different temperatures and $p(H_2O)_{ATM}$ values. Notably, the kinetic parameters determined by the conventional kinetic analysis are only empirically significant. For example, they can be used to replicate the experimentally recorded kinetic curves at each $p(H_2O)_{ATM}$ value. However, they cannot be directly correlated with the intrinsic kinetics of the reaction from a physico-chemical perspective. It is therefore essential to consider the effect of water vapor in the kinetic equation in order to achieve a universal description of the kinetic behavior as a function of temperature, α, and $p(H_2O)$, and to obtain the kinetic parameters that are physico-chemically relevant.

3.4 Extended kinetic analysis considering the effect of water vapor

Incorporation of an AF of $p(H_2O)$ and the equilibrium pressure of the reaction ($P_{eq}(T)$), *i.e.*, $h(p(H_2O), P_{eq}(T))$, into the fundamental kinetic equation is one way to account for the effect of $p(H_2O)$ on the kinetics. The temperature dependence of $P_{eq}(T)$ is expressed as follows:

$$P_{eq}(T) = \exp\left(-\frac{\Delta_r G^\circ}{RT}\right) = \exp\left(-\frac{\Delta_r H^\circ - T\Delta_r S^\circ}{RT}\right), \qquad (8)$$

where $\Delta_r G^\circ$, $\Delta_r H^\circ$, and $\Delta_r S^\circ$ are the standard Gibbs energy, enthalpy change, and entropy change of the reaction, respectively. The $P_{eq}(T)$ values of the thermal dehydration of SC-MH at different temperatures are shown in Fig. S12 (ESI†), together with the range of (T, $p(H_2O)_{ATM}$) values of the experimental kinetic curves obtained in this study. The thermal dehydration of SC-MH occurs at higher temperatures than the equilibrium temperature at a fixed $p(H_2O)$ and at lower $p(H_2O)$ values than the equilibrium pressure at a fixed temperature. For the IP process, the extended kinetic equation is

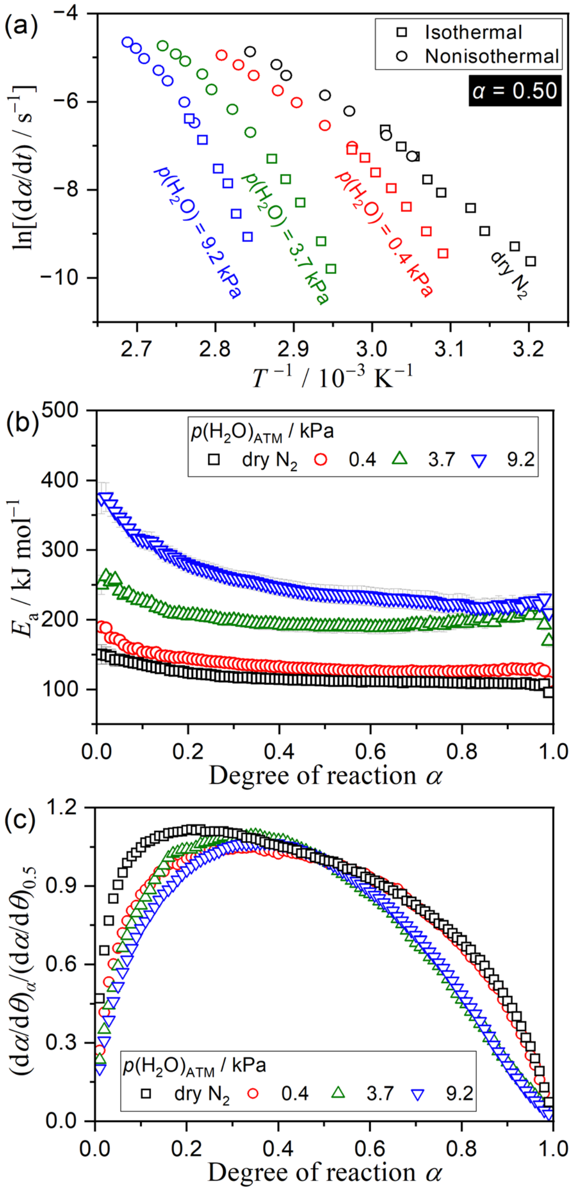

Fig. 4 Comparison of the results of the conventional kinetic analysis of the thermal dehydration of SC-MH under different atmospheric conditions in a stream of dry or wet N$_2$ with different $p(H_2O)_{ATM}$ values: (a) Friedman plots at α = 0.50, (b) apparent E_a values at different α values, and (c) normalized experimental master plots of $(d\alpha/d\theta)_\alpha/(d\alpha/d\theta)_{0.50}$ *versus* α.

expressed as follows.[24,25,27,28,32–34]

$$\frac{1}{t_{IP}} = A_{IP}\exp\left(-\frac{E_{a,IP}}{RT}\right)f(\alpha_{IP})h\left(p(H_2O), P_{eq}(T)\right) \qquad (9)$$

Recently, Koga *et al.* proposed an analytical form of the AF based on the classical nucleation and interfacial reaction theory, which includes various elementary steps.[24–38]

$$h\left(p(H_2O), P_{eq}(T)\right) = \left(\frac{1}{p(H_2O)}\right)^a\left[1-\left(\frac{p(H_2O)}{P_{eq}(T)}\right)^b\right], \qquad (10)$$

where all pressure terms are in the unit of bar. The AF in eqn (10) has been derived on the assumption that the rate-determining step occurs in an elementary step among the consecutive/concurrent steps, as well as the steady-state assumption for the other elementary steps. The exponents (a, b) in the AF originally relate to the elementary steps selected as the rate-determining step and can have values of (0, 1), (1, 1), or $a = b$. The derivation of the analytical form of AF is briefly described in the ESI† (Section S5), as exemplified by the case of the thermal dehydration of SC-MH (Tables S5 and S6, ESI†). The extended Arrhenius plot for the IP is expressed as follows:

$$\ln\left[\frac{\left(\frac{1}{t_{IP}}\right)(p(H_2O))^a}{1-\left(\frac{p(H_2O)}{P_{eq}(T)}\right)^b}\right] = \ln[A_{IP}f(\alpha_{IP})] - \frac{E_{a,IP}}{RT} \qquad (11)$$

When the appropriate values of (a, b) are employed, the plot of the left-hand side of eqn (11) *versus* reciprocal temperature should yield a single straight line for all data points recorded at disparate temperatures and $p(H_2O)_{ATM}$ values. Fig. S13 (ESI†) illustrates the extended Arrhenius plots with (a, b) = (0, 1) and (1, 1) for the IP process. When the values of (a, b) were set to (0, 1) and (1, 1), it was not possible to achieve a single straight line on the extended Arrhenius plots by exhibiting the individual linear correlations of the data points at each $p(H_2O)_{ATM}$ value. Besides, the optimization of the $a = b$ value yielded a single straight line, with the resulting value being $a = b = 2.70$, as shown in Fig. 5. With $a = b = 2.70$, all data points at $p(H_2O)_{ATM}$ = 0.4, 3.6, and 8.9 form a straight line in the extended Arrhenius coordinate (Fig. 5(a)). This yielded the apparent ($E_{a,IP}$/kJ mol^{-1}, $\ln(A_{IP}/s^{-1})$) values of (297.3 ± 10.2, 87.6 ± 3.6). The apparent Arrhenius parameters appear to replicate the experimental data points of the IP process at varying temperatures and $p(H_2O)_{ATM}$ values (Fig. 5(b)).

The mass loss process of the thermal dehydration of SC-MH under various temperatures and $p(H_2O)_{ATM}$ values can also be analyzed using an extended kinetic equation with the AF of $h(p(H_2O), P_{eq}(T))$.[24–38]

$$\frac{d\alpha}{dt} = A\exp\left(-\frac{E_a}{RT}\right)f(\alpha)h\left(p(H_2O), P_{eq}(T)\right) \qquad (12)$$

As with the IP process, the analytical form of AF presented in eqn (10) can be derived for the mass loss process based on the classical surface nucleation and interfacial reaction theories (Section S5, ESI†). Upon taking logarithms after incorporating eqn (10) into eqn (12), the extended kinetic equation for the Friedman plot is obtained.

$$\ln\left[\frac{\left(\frac{d\alpha}{dt}\right)(p(H_2O))^a}{1-\left(\frac{p(H_2O)}{P_{eq}(T)}\right)^b}\right] = \ln[Af(\alpha)] - \frac{E_a}{RT} \qquad (13)$$

The exponents (a, b) in AF have particular physico-chemical implications when they are equal to (0, 1), (1, 1), or $a = b$ in both surface and interfacial reactions. Fig. 6 illustrates the extended Friedman plots at α = 0.50, which have been examined with different pairs of (a, b) values in AF. The extended Friedman plot with (a, b) = (0, 1) exhibited different linear correlations for

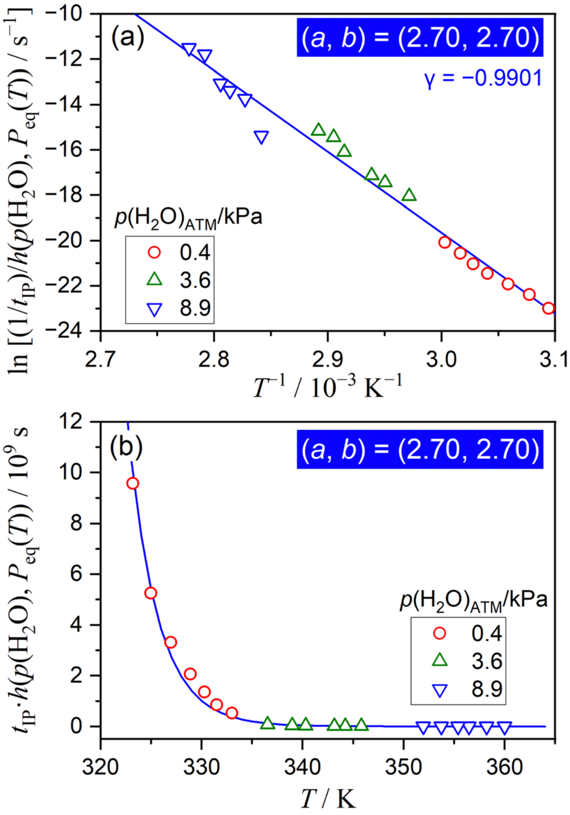

Fig. 5 Results of the extended Arrhenius plot for the IP process of the thermal dehydration of SC-MH under isothermal conditions in a stream of wet N_2 with different $p(H_2O)_{ATM}$ values, examined according to eqn (11) with $a = b = 2.70$: (a) extended Arrhenius plot and (b) the comparison between the experimental data point and the replicated curve using the apparent kinetic parameters determined by the extended Arrhenius plot.

the data points at individual $p(H_2O)_{ATM}$ values (Fig. 6(a)). With $(a, b) = (1, 1)$, the extended Friedman plot exhibited an approximate linear correlation over different temperatures and $p(H_2O)_{ATM}$ values (Fig. 6(b)). The optimization of the $a = b$ value to obtain the optimal linear correlation of the extended Friedman plot resulted in $a = b = 1.20$ (Fig. 6(c)), which exhibited a slight improvement in the linear correlation of the plot in comparison with that with $(a, b) = (1, 1)$. Notably, the optimized $a = b$ value is approximately equal to unity. In theory, the interfacial reaction described by $(a, b) = (1, 1)$ is understood to be controlled by the creation of a water vacancy at the reaction interface. It is also anticipated that the values $a = b$, including $(a, b) = (1, 1)$, will be observed for the reaction that is controlled by the creation of a building unit of Na_2CO_3. However, the extended Friedman plot over different temperatures and $p(H_2O)_{ATM}$ values still exhibited a convex curvature within the data points at individual $p(H_2O)_{ATM}$ values.

In order to refine the extended Friedman plot applied over a range of temperatures and $p(H_2O)_{ATM}$ values, it is necessary to take into account the potential contribution of the $p(H_2O)_{SG}$. Indeed, the considerable impact of $p(H_2O)_{SG}$ on the mass loss process has been anticipated based on the variations in the kinetic data with respect to the m_0 and q_v of inert gas for the thermal dehydration of SC-MH in a stream of dry N_2 gas (Fig. S5 and S6, ESI†). Although the actual value of $p(H_2O)_{SG}$ at the reaction interface cannot be measured during the thermal dehydration process, it is anticipated that the value is proportional to the rate of water vapor evolution at the reaction interface. Consequently, the effective $p(H_2O)$ ($p(H_2O)_{EF}$), which considers the contributions of both $p(H_2O)_{SG}$ and $p(H_2O)_{ATM}$, can be introduced in the extended kinetic equation as an empirical procedure for accounting for the $p(H_2O)_{SG}$.[32,36–38]

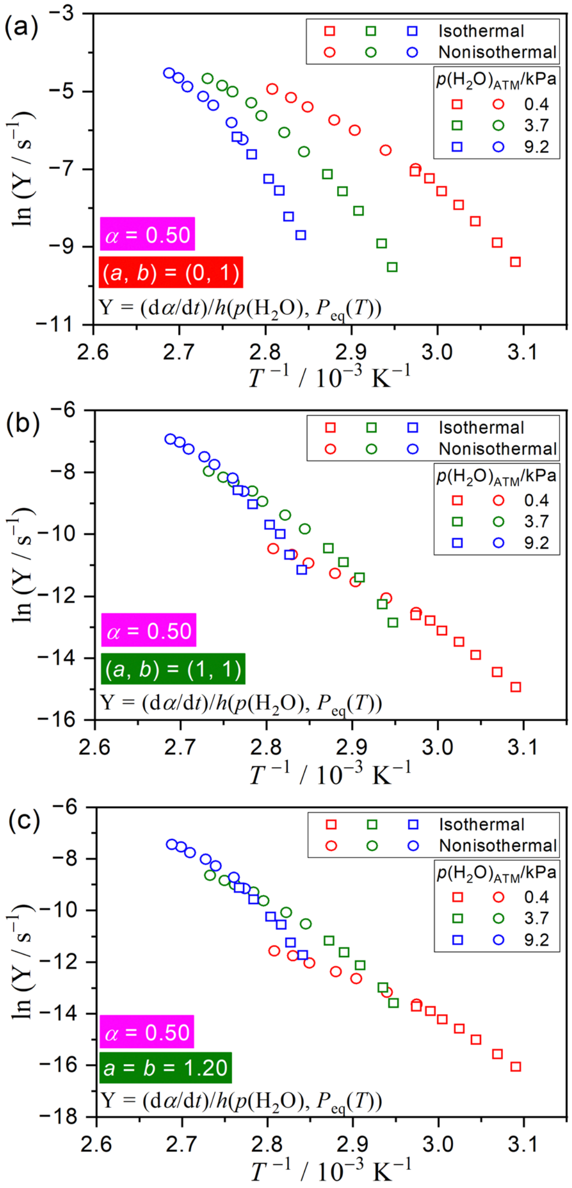

Fig. 6 Extended Friedman plots at α = 0.50 for the mass loss process of the thermal dehydration of SC-MH under isothermal and linear nonisothermal conditions in a stream of wet N_2 with various $p(H_2O)_{ATM}$ values, examined according to eqn (13) with different pairs of (a, b) in the AF: (a) (0, 1), (b) (1, 1), and (c) $a = b = 1.20$.

$$p(H_2O)_{EF} = p(H_2O)_{SG} + d \cdot p(H_2O)_{ATM} = c \cdot \left(\frac{d\alpha}{dt}\right) + d \cdot p(H_2O)_{ATM}, \tag{14}$$

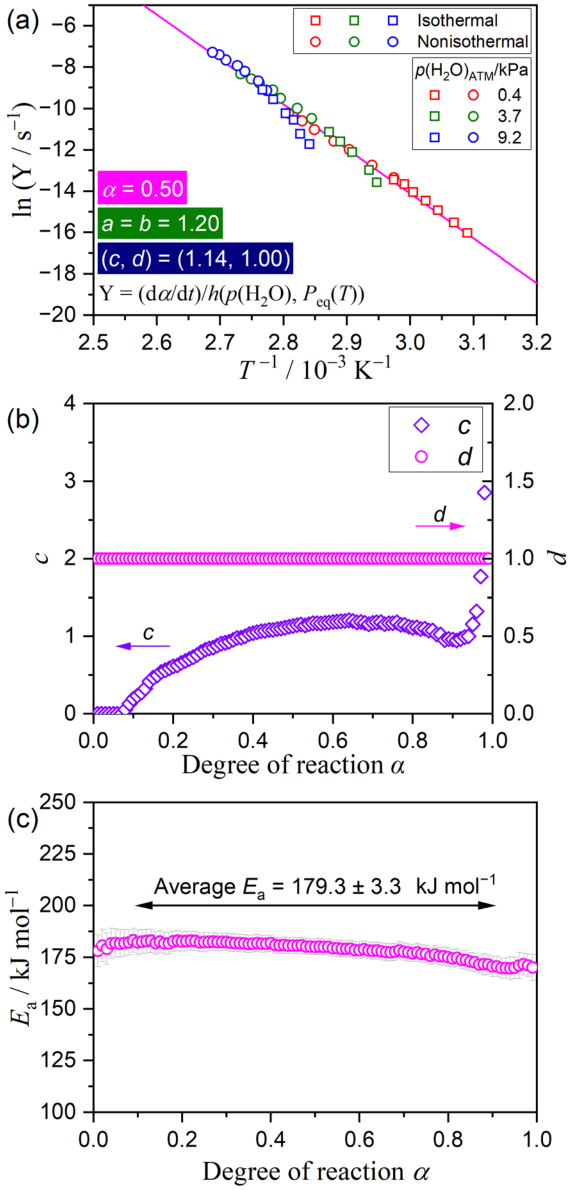

Fig. 7 Results of the extended Friedman plots considering $p(H_2O)_{EF}$ for the mass loss process of the thermal dehydration of SC-MH over the conditions in a stream of wet N_2 with $p(H_2O)_{ATM}$ = 0.4, 3.7, and 9.2 kPa: (a) the extended Friedman plot at α = 0.50 with (*a*, *b*, *c*, *d*) = (1.20, 1.20, 1.14, 1.00), (b) optimized coefficients (*c*, *d*) at various α values, and (c) apparent E_a values at various α values.

where the coefficients (*c*, *d*) describe the contribution of $p(H_2O)_{SG}$ and $p(H_2O)_{ATM}$, respectively. The extended Friedman plots at varying α values were subjected to a comprehensive reevaluation, wherein the (*c*, *d*) values were optimized while the exponents in AF were maintained at $a = b = 1.20$. Fig. 7 illustrates the results of the refinement of the extended Friedman plot. The linear correlation of the extended Friedman plot was enhanced at each α value with optimized (*c*, *d*) values (Fig. 7(a)). The optimized (*c*, *d*) values demonstrated disparate variation trends (Fig. 7(b)). The *c* value was negligible at the initial reaction stage, which corresponds to the SR process ($\alpha < 0.1$), where the diffusional removal of the self-generated water vapor takes place immediately. Subsequently, the *c* value increased gradually to unity in the main reaction stage controlled by PBR. In this stage, the diffusion of the self-generated water vapor *via* the surface product layer was the necessary process for the mass loss process. In the final reaction stage ($\alpha > 0.9$), the *c* value rapidly increased, indicating the difficulty of removing the self-generated water vapor from the particle center. Besides, the coefficient *d* for $p(H_2O)_{ATM}$ remained constant throughout the course of the reaction. The apparent E_a values determined by optimizing (*c*, *d*) values exhibited approximately constant values with an average value of 179.3 ± 3.3 kJ mol^{-1} ($0.10 \le \alpha \le 0.90$) (Fig. 7(c)).

The extended isoconversional kinetic approach, which considers both the effect of $p(H_2O)_{SG}$ and $p(H_2O)_{ATM}$, can be used to incorporate the kinetic data recorded in a stream of dry N_2, as the $p(H_2O)_{EF}$ value is equivalent to $p(H_2O)_{SG}$. This procedure broadens the temperature and $p(H_2O)$ ranges encompassed by the universal kinetic description. Notably, this procedure is not applicable to the IP process due to the absence of the self-generated water vapor. Fig. 8 depicts the results of the kinetic analysis based on the extended kinetic equation (eqn (12)), which considers the effect of $p(H_2O)_{EF}$ (eqn (14)), reexamined by incorporating the kinetic data recorded in a stream of dry and wet N_2. The preceding results of (*a*, *b*, *c*, *d*) were used as the initial values, and the coefficient *c* was optimized to achieve the most optimal linear correlation of the extended Friedman plot at individual α values, encompassing all data points recorded under disparate atmospheric conditions. By optimizing the *c* value, a statistically significant linear correlation was achieved for the extended Friedman plot, including the data point for the reactions in a stream of dry N_2 (Fig. 8(a)), which was observed at various α values during the reaction (Fig. 8(b)). The optimized *c* values at different α values were larger than those previously optimized for the reactions in a stream of wet N_2 (Fig. 8(c)), although the variation trend as the reaction proceeded was similar. The apparent E_a values were also slightly larger than those determined for the reactions in a stream of wet N_2 and exhibited a gradual decrease as the reaction proceeded (Fig. 8(c)). However, the average E_a value within the major stage of the reaction ($0.10 \le \alpha \le 0.90$) indicated an acceptable standard deviation: E_a = 203.4 ± 4.2 kJ mol^{-1}. It is important to acknowledge that enhancing the extended Friedman plot can be achieved through the optimization of $a = b$ values at each α value, followed by the repetition of the optimization of $a = b$ and *c* values. However, this approach led to variations in $a = b$ values as the reaction progressed and increases in $a = b$ and *c* values as the optimization calculation was repeated. In the interest of maintaining the simplicity of the kinetic modeling in the context of a universal kinetic approach, the initial optimization results assuming a constant $a = b$ value during the reaction are reported herein.

Assuming that the overall reaction is characterized by the average E_a value, the experimental master plots based on the extended kinetic equation (eqn (12)) can be obtained by

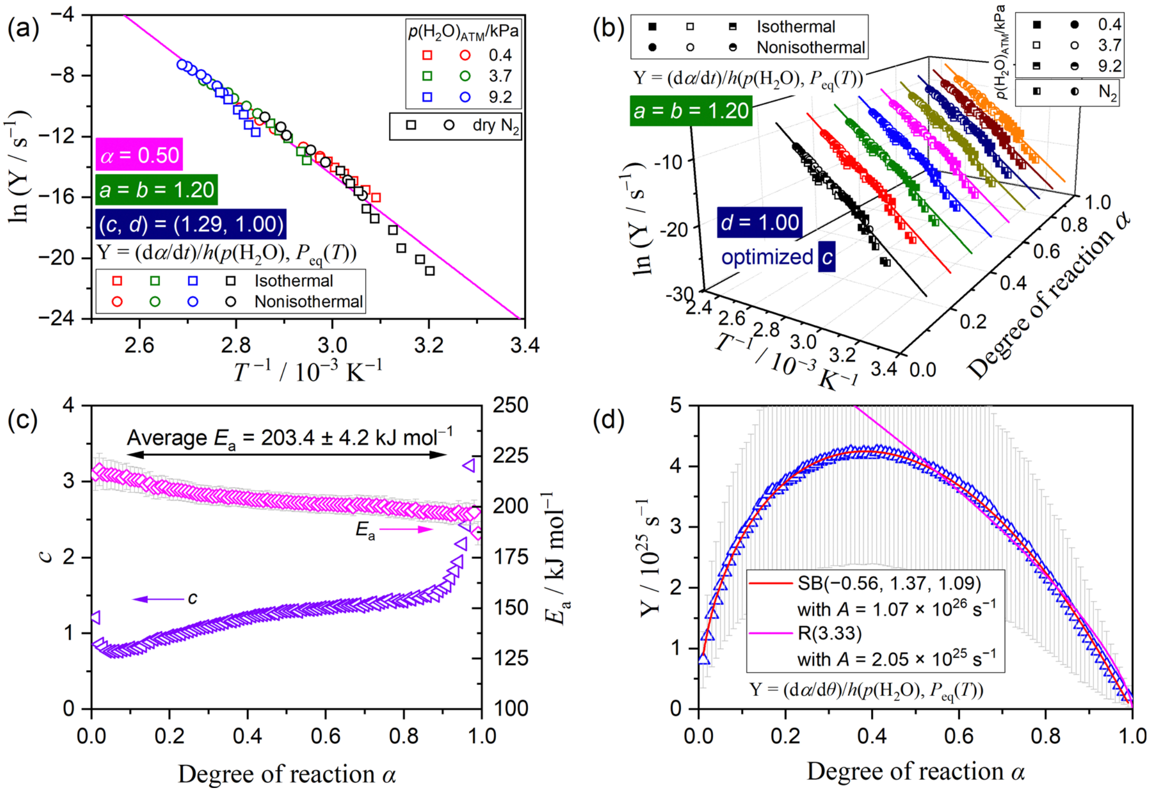

Fig. 8 Results of the kinetic analysis based on the extended kinetic equation (eqn (12)) considering $p(H_2O)_{EF}$ (eqn (14)) for the mass loss process of the thermal dehydration of SC-MH over different atmospheric conditions in a stream of dry and wet N_2 with different $p(H_2O)_{ATM}$ values: (a) the extended Friedman plot at α = 0.50, (b) the extended Friedman plots at various α values, (c) the optimized c and apparent E_a values at various α values, and (d) the extended experimental master plot.

calculating $(d\alpha/d\theta)/h(p(H_2O), P_{eq}(T))$ at each α.[29,32,36–38]

$$\frac{\left(\frac{d\alpha}{d\theta}\right)}{h(p(H_2O), P_{eq}(T))} = \frac{\left(\frac{d\alpha}{dt}\right)\exp\left(\frac{E_a}{RT}\right)}{h(p(H_2O), P_{eq}(T))} = Af(\alpha) \qquad (15)$$

The extended experimental master plot demonstrated the maximum reaction rate occurred at the midpoint of the reaction at α = 0.41 (Fig. 8(d)). Notably, the shape of the extended experimental master plot, which universally describes the rate behavior across different temperatures and $p(H_2O)_{EF}$ values, is similar to the conventional experimental master plots constructed for the reactions at each $p(H_2O)_{ATM}$ value (Fig. 4(c)). Therefore, the physico-geometrical reaction scheme, as described by a consecutive process comprising SR and PBR, is also anticipated from the extended kinetic approach. According to eqn (15), the extended experimental master plot was fitted using the SB(m, n, p) model (eqn (6)), resulting in optimized kinetic exponents SB(-0.56 ± 0.14, 1.37 ± 0.06, 1.09 ± 0.13) and A value of $(1.07 \pm 0.01) \times 10^{26}$ s^{-1}. The fitting of the deceleration stage of the extended experimental master plot ($0.45 \leq \alpha \leq 0.95$) using R($n$) (eqn (7)) resulted in $n = 3.33 \pm 0.19$ and $A = (2.05 \pm 0.09) \times 10^{25}$ s^{-1}, indicating the 3D interface shrinkage.

In interpreting the results of the extended kinetic approach, two points require particular attention. It is important to note that the exponents (a, b) in AF (eqn (10)) and the coefficients (c, d) in $p(H_2O)_{EF}$ (eqn (14)) can be varied according to the sample, sampling, and reaction conditions. Such factors include, for instance, the sample particle size, the m_0 used to collect kinetic data, and the q_v of the purge gas during the reaction. These factors modify the physico-geometrical constraints of the reaction, both within each sample particle and within the reaction system. This alters the effect of $p(H_2O)_{SG}$ and $p(H_2O)_{ATM}$ on the reaction kinetics. However, if we consider this from the opposite perspective, it may be feasible to parameterize the influence of these empirical factors on the kinetics using the exponents (a, b) and coefficients (c, d).

Secondly, the significance of the apparent Arrhenius parameters (E_a, A) determined by the extended kinetic approach warrants further consideration. The apparent (E_a, A) values determined by the extended kinetic approach over different temperatures and $p(H_2O)$ values are typically larger than those determined by the conventional kinetic approach to the reaction in a stream of dry N_2. This is due to the fact that the extended Arrhenius-type plots, including the extended Friedman plot, simultaneously examine the temperature dependence of both the rate constant based on the Arrhenius equation and of the equilibrium constant based on the van't Hoff equation. Notably, the contribution of the temperature dependence of the equilibrium constant is multiplied by the exponent b in AF. Consequently, the temperature dependence of the rate constant in the extended kinetic equation can be obtained by subtracting the contribution of the temperature dependence of the equilibrium constant. To illustrate, the extended Friedman plot yields the following equation by subtracting the van't Hoff plot (logarithmic form of eqn (8)) multiplied by the b value.[36–38]

$$\ln\left[\left(\frac{\mathrm{d}\alpha}{\mathrm{d}t}\right)\frac{p(\mathrm{H_2O})^a}{P_{\mathrm{eq}}(T)^b - p(\mathrm{H_2O})^b}\right] = -\frac{E_\mathrm{a} - b\Delta_\mathrm{r}H^\circ}{RT} + \ln\left[Af(\alpha)\exp\left(-\frac{b\Delta_\mathrm{r}S^\circ}{R}\right)\right] \tag{16}$$

If the $p(\mathrm{H_2O})^a/(P_{\mathrm{eq}}(T)^b - p(\mathrm{H_2O})^b)$ term can be approximated to be unity, the intrinsic Arrhenius parameters can be obtained by the following equations:[36,38]

$$E_{\mathrm{a,int}} \approx E_\mathrm{a} - b\Delta_\mathrm{r}H^\circ \tag{17}$$

$$A_{\mathrm{int}} \approx A\exp\left(-\frac{b\Delta_\mathrm{r}S^\circ}{R}\right) \tag{18}$$

According to eqn (17) and (18), the intrinsic Arrhenius parameters ($E_{\mathrm{a,IP,int}}$/kJ mol^{-1}, $\ln(A_{\mathrm{IP,int}}/\mathrm{s}^{-1})$) for the IP process were determined to be (139.1 ± 10.2, 37.1 ± 3.6) using the values ($\Delta_\mathrm{r}H^\circ_{298}$/kJ mol^{-1}, $\Delta_\mathrm{r}S^\circ_{298}$/J (mol K)$^{-1}$) of (58.6, 155.4).[45] Similarly, the intrinsic Arrhenius parameters ($E_{\mathrm{a,int}}$/kJ mol^{-1}, A_{int}/s^{-1}) were calculated, yielding the values of (133.1 ± 4.2, (1.95 ± 0.01) × 10^{16}).

3.5 Effect of water vapor on the individual physico-geometrical reaction steps

The results of the extended kinetic approach, which considered the effect of water vapor on the IP and mass loss processes, indicated that the physico-geometrical consecutive process, comprising the IP, SR, and PBR, may be suitable for describing the thermal dehydration of SC-MH in a stream of dry and wet $\mathrm{N_2}$. Fig. 9 depicts SEM images of partially dehydrated sample particles under isothermal conditions at 313 K in a stream of dry $\mathrm{N_2}$. During the IP (Fig. 9(a)), the surface morphology remained unchanged from that of the original sample particles (Fig. S4, ESI†). Immediately following the onset of mass loss, the particle surfaces exhibited a roughened texture, with the emergence of small protruding crystals radiating from the particle surfaces (Fig. 9(b)). This observation indicated that the mass loss process had initiated *via* the SR. As the reaction proceeded, the surface became increasingly rough (Fig. 9(c) and (d)). At this stage, the particle surface exhibited the emergence of several pores, which may serve as a diffusion path for the water vapor generated at the internal reaction interface of the PBR. Upon completion of the mass loss process, the product particles displayed rough surfaces while maintaining the protruding crystals on the surfaces (Fig. 9(e)). The changes in the surface morphology throughout the thermal dehydration of SC-MH support the physico-geometrical consecutive process of IP–SR–PBR.

Based on the Mampel's model,[56,82,83] differential kinetic equations of the IP–SR–PBR(n) models with distinct shrinkage

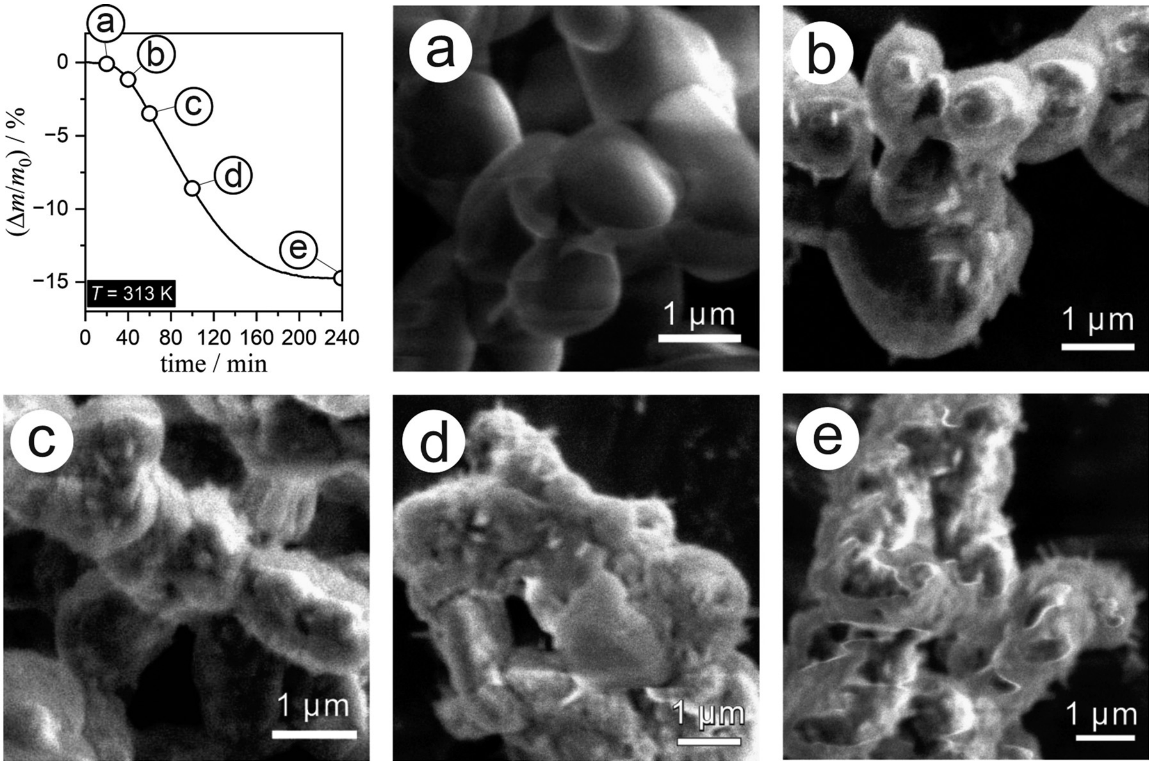

Fig. 9 SEM images of partially dehydrated sample particles under isothermal conditions at 313 K in a stream of dry $\mathrm{N_2}$ for different duration times: (a) 20 min (α = 0.01), (b) 40 min (α = 0.17), (c) 60 min (α = 0.38), (d) 100 min (α = 0.60), and (e) 240 min (α = 1.00).

dimension *n* of the reaction interface for the PBR have been derived by Ogasawara and Koga (Table S7, ESI†).[56] The individual kinetic data recorded under isothermal conditions at different temperatures in a stream of dry or wet N_2 with varying $p(H_2O)_{ATM}$ values (Fig. 1) were fitted using these kinetic equations. This was achieved through the optimization of t_{IP} and rate constants for the SR and PBR(*n*) processes (k_{SR} and $k_{PBR(n)}$) *via* nonlinear least-squares analysis with the Levenberg–Marquardt algorithm. The model fitting indicated that the IP–SR–PBR(*n*) model with the two-dimensional interface shrinkage for the PBR (*i.e.*, IP–SR–PBR(2)) was the most suitable model. Fig. 10 illustrates the typical model fitting results obtained with the IP–SR–PBR(2) model for the reactions under isothermal conditions at different $p(H_2O)_{ATM}$ values. Table S8 (ESI†) lists the optimized t_{IP}, k_{SR}, and k_{PBR} values based on the IP–SR–PBR(2) model at different temperatures and $p(H_2O)_{ATM}$ values.

The temperature dependence of $1/t_{IP}$, k_{SR}, and $k_{PBR(2)}$ was initially examined using the conventional Arrhenius plot.

$$\ln k = \ln A - \frac{E_a}{RT} \tag{19}$$

In all physico-geometrical reaction steps, the conventional Arrhenius plot yielded disparate linear correlations for the rate constants determined at varying $p(H_2O)_{ATM}$ values, as illustrated in Fig. S14 (ESI†). Table S9 (ESI†) lists the apparent Arrhenius parameters for the individual physico-geometrical reaction steps at each $p(H_2O)_{ATM}$ value. Regardless of the physico-geometrical reaction step, both E_a and $\ln A$ values exhibited a consistent trend of increase with increasing $p(H_2O)_{ATM}$ value.

A universal kinetic description for individual physico-geometrical reaction steps was examined for the reactions in a stream of wet N_2 with different $p(H_2O)_{ATM}$ values by introducing AF in eqn (10) into eqn (19).[24–29,32,34–38]

$$\ln\left[\frac{k\left(p(H_2O)\right)^a}{1-\left(\frac{p(H_2O)}{P_{eq}(T)}\right)^b}\right] = \ln A - \frac{E_a}{RT} \tag{20}$$

It should be noted that the physicochemical features of the specific physico-geometrical reaction step have been considered in the AF and characterized by the exponents (*a*, *b*). Therefore, the kinetic analysis based on eqn (20) for each IP, SR, and PBR process reveals the physicochemical features of the specific physico-geometrical reaction step, simultaneously with the universal kinetic description over different temperatures and $p(H_2O)$ values.

In all physico-geometrical reaction steps, the extended Arrhenius plot demonstrated a statistically significant linear correlation, including all data points at varying $p(H_2O)_{ATM}$ values, as illustrated in Fig. S15 (ESI†). Table 1 lists the apparent kinetic parameters of *a* = *b*, E_a, and $\ln A$, as determined for the individual physico-geometrical reaction steps. The apparent kinetic parameters for IP were found to be significantly reduced in comparison with those determined using the t_{IP} values, which were defined empirically as the

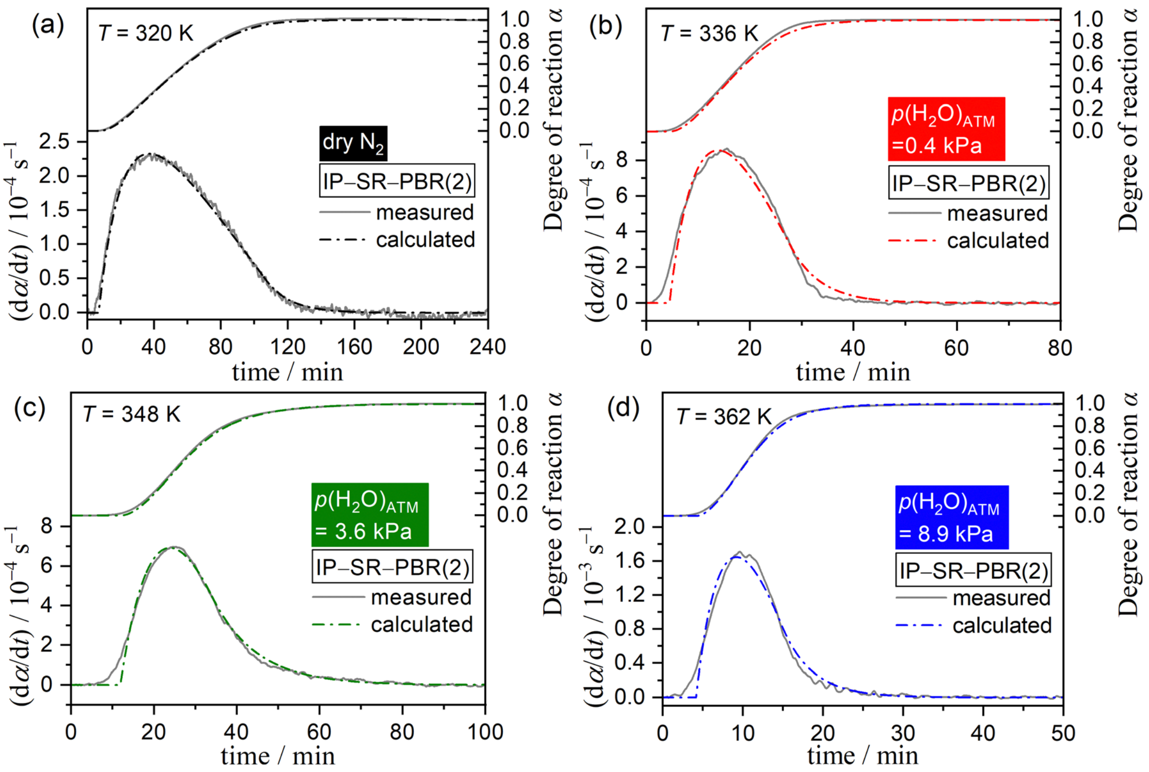

Fig. 10 Typical fitting results of the IP–SR–PBR(2) model to the thermal dehydration of SC-MH under isothermal conditions in a stream of (a) dry N_2, (b) wet N_2 with $p(H_2O)_{ATM}$ = 0.4 kPa, (c) wet N_2 with $p(H_2O)_{ATM}$ = 3.6 kPa, and (d) wet N_2 with $p(H_2O)_{ATM}$ = 8.9 kPa.

Table 1 Apparent kinetic parameters of $a = b$, E_a, and $\ln A$ and the intrinsic kinetic parameters of $E_{a,int}$ and $\ln A_{int}$ for the IP, SR, and PBR(2) processes of the thermal dehydration of SC-MH in a stream of wet N_2 with different $p(H_2O)_{ATM}$ values, determined according to eqn (20) with the AF in eqn (10)

		Apparent kinetic parameter			Intrinsic kinetic parameter[b]	
Process	$a = b$	E_a/kJ mol^{-1}	$\ln(A/s^{-1})$	$-\gamma$[a]	$E_{a,int}$/kJ mol^{-1}	$\ln(A_{int}/s^{-1})$
IP	2.17	237.4 ± 8.8	67.9 ± 3.1	0.9893	110.1 ± 8.8	27.3 ± 3.1
SR	1.91	230.9 ± 6.4	66.6 ± 2.3	0.9939	119.0 ± 6.4	30.9 ± 2.3
PBR(2)	1.63	211.2 ± 7.7	59.8 ± 2.7	0.9897	115.9 ± 7.7	29.3 ± 2.7

[a] Correlation coefficient of the linear regression analysis. [b] Calculated according to eqn (17) and (18) using $\Delta_r H^\circ_{298} = 58.6$ kJ mol^{-1} and $\Delta_r S^\circ_{298} = 155.4$ J (mol K)$^{-1}$.

duration until the mass loss reached 2 μg (Fig. 5). In contrast, the E_a and $\ln A$ values for the SR and PBR(2) processes exhibited larger values in comparison with those determined by the extended Friedman plot (Fig. 7 and 8). It is noteworthy that all kinetic parameters, including $a = b$, E_a, and $\ln A$, exhibited a systematic decrease as the reaction steps progressed from IP to PBR(2) *via* SR.

To further extend the universal kinetic approach, SR and PBR(2) processes were reanalyzed by considering $p(H_2O)_{EF}$ in eqn (14) and by optimizing the coefficients (c, d), where the kinetic data recorded in a stream of dry N_2 were additionally included for the analysis. It should be noted that the IP process was excluded from the reanalysis since water vapor is not produced during IP. Fig. 11 illustrates the extended Arrhenius plots, with the consideration of $p(H_2O)_{EF}$ for the SR and PBR(2) processes. In both the SR and PBR(2) processes, the extended Arrhenius plot, which considered $p(H_2O)_{EF}$, yielded a statistically significant linear correlation that include all data points originating from the reactions in a stream of dry and wet N_2 with different $p(H_2O)_{ATM}$ values. Table 2 lists the apparent kinetic parameters obtained by the extended Arrhenius plots for the SR and PBR(2) processes. Notably, the coefficient c in the $p(H_2O)_{EF}$ increased significantly as the reaction step progressed from SR to PBR(2), indicating that the self-generated water vapor plays a more prominent role in the PBR(2) process. This finding can be explained by the distinct physico-geometrical constraints of the SR and PBR(2) processes with regard to the removal of the self-generated water vapor. The reaction sites during SR are directly exposed to the reaction atmosphere, allowing for the straightforward removal of the evolved water vapor from the reaction sites. In contrast, the diffusion of water vapor through the surface product layer is necessary for the removal of self-generated water vapor at the internal reaction interface during the PBR(2) process. Although the apparent E_a and $\ln A$ values determined by incorporating $p(H_2O)_{EF}$ and including the data points in a stream of dry N_2 were larger than those determined by the extended Arrhenius plot with $p(H_2O)_{ATM}$ and without data points in a stream of dry N_2, the observed trend of decreasing the Arrhenius parameters with reaction step advancement from SR to PBR(2) remained consistent. Notably, the Arrhenius parameters listed in Table 2 cover the universal kinetic description of the reactions in wider $p(H_2O)$ and temperature ranges.

The apparent Arrhenius parameters determined for the individual reaction step in the IP–SR–PBR scheme by the extended Arrhenius plot can also be correlated to the individual intrinsic values. The intrinsic Arrhenius parameters calculated based on eqn (17) and (18) are listed in Tables 1 and 2. The intrinsic Arrhenius parameters calculated from the apparent kinetic parameters obtained by the extended Arrhenius plot with $p(H_2O)_{ATM}$ without data points in a stream of dry N_2 were practically identical among distinct reaction steps with reference to the standard error of each value (Table 1). The intrinsic Arrhenius parameters determined by considering $p(H_2O)_{EF}$ and including the data points in a stream of dry N_2 were found to be larger than those determined without considering $p(H_2O)_{SG}$ and without data points in a stream of dry N_2 (Table 2). Furthermore, the intrinsic Arrhenius parameters for the SR process were found to be markedly larger than those for the PBR(2) process. The discrepancy between the results of the

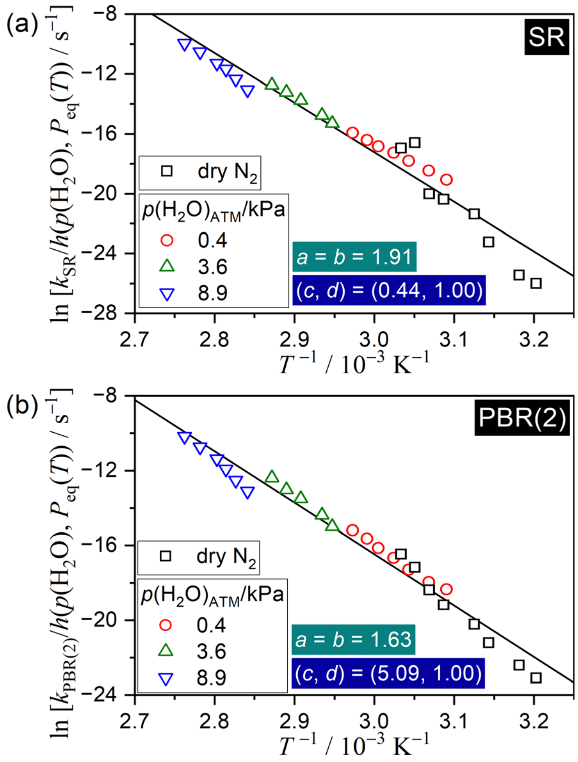

Fig. 11 Extended Arrhenius plots for SR and PBR(2) processes of the thermal dehydration of SC-MH in a stream of dry or wet N_2 with different $p(H_2O)_{ATM}$ values, examined according to eqn (20) with the AF in eqn (10) and considering $p(H_2O)_{EF}$ in eqn (14): (a) SR and (b) PBR(2).

Table 2 Apparent kinetic parameters of $a = b$, E_a, and $\ln A$ and the intrinsic kinetic parameters of $E_{a,int}$ and $\ln A_{int}$ for the SR and PBR(2) processes of the thermal dehydration of SC-MH in a stream of dry and wet N_2 with different $p(H_2O)_{ATM}$ values, determined according to eqn (20) with the AF in eqn (10) and by considering $p(H_2O)_{EF}$ in eqn (14)

				Apparent kinetic parameter			Intrinsic kinetic parameter[b]	
Process	$a = b$	c	d	E_a/kJ mol^{-1}	$\ln(A/s^{-1})$	$-\gamma$[a]	$E_{a,int}$/kJ mol^{-1}	$\ln(A_{int}/s^{-1})$
SR	1.91	0.44	1.00	275.6 ± 13.7	82.2 ± 5.0	0.9716	163.6 ± 13.7	46.5 ± 5.0
PBR(2)	1.63	5.09	1.00	228.6 ± 8.0	66.0 ± 2.9	0.9858	133.2 ± 8.0	35.6 ± 2.9

[a] Correlation coefficient of the linear regression analysis. [b] Calculated according to eqn (17) and (18) using $\Delta_r H^\circ_{298} = 58.6$ kJ mol^{-1} and $\Delta_r S^\circ_{298} = 155.4$ J (mol K)$^{-1}$.

extended Arrhenius plots with different calculation conditions may suggest that the reactions occurring at lower $p(H_2O)_{ATM}$ values are more sensitive to $p(H_2O)_{SG}$. Moreover, this phenomenon is particularly pronounced in the context of the SR process. These were anticipated based on the shift trend of the TA curves to higher temperatures with increasing $p(H_2O)_{ATM}$ (Fig. S9, ESI†), where the shift width with increasing $p(H_2O)_{ATM}$ was larger at a lower $p(H_2O)_{ATM}$ region. Additionally, the shift wide of the onset temperature with $p(H_2O)_{ATM}$ was larger than that of the peak top temperature. Furthermore, a distinctive shape was observed in the conventional experimental master plot for the reactions in a stream of dry N_2 in comparison with those in the presence of atmospheric water vapor (Fig. 4(c)), indicating that the maximum reaction rate is attained at a smaller α value. The observed phenomenon of the effect of $p(H_2O)_{SG}$ and $p(H_2O)_{ATM}$ indicates that $p(H_2O)_{SG}$ plays an important role in regulating the kinetic behavior of the thermal dehydration of SC-MH, particularly for reactions in a stream of dry N_2 and at a lower $p(H_2O)_{ATM}$. This also describes the changes in the kinetic behaviors with m_0 and q_v in a stream of dry N_2.

4. Conclusions

The thermal dehydration kinetics of SC-MH were significantly affected by m_0 and q_v in a stream of dry N_2 due to the influence of the self-generated water vapor. An increase in m_0 and a decrease in q_v resulted in a deceleration of the overall reaction rate. In addition, a systematic variation in the kinetics was observed when the $p(H_2O)_{ATM}$ value of the purge gas was varied, exhibiting a deceleration as the $p(H_2O)_{ATM}$ value increased. Therefore, both $p(H_2O)_{SG}$ and $p(H_2O)_{ATM}$ are the parameters that determine the apparent kinetics of the reaction. The application of the conventional kinetic approach as a function of temperature and α to such a reaction process yielded apparent kinetic results that were only useful for reproducing the kinetic behaviors of the reaction under specific reaction conditions of m_0, q_v, and $p(H_2O)_{ATM}$. Additionally, a particular physico-geometrical reaction characteristic was anticipated for the reaction, as evidenced by the appearance of IP and the subsequent sigmoidal mass loss curves recorded under isothermal conditions. This can be described by consecutive physico-geometrical steps of IP, SR and PBR. In order to elucidate the kinetics of thermal dehydration of SC-MH across diverse temperatures and $p(H_2O)$ values, a comprehensive kinetic approach was conducted in a stepwise manner. This approach comprised four steps: (1) development of a universal kinetic description across varying temperatures and $p(H_2O)_{ATM}$ values, (2) incorporation of the effect of self-generated water vapor into the universal kinetic description, (3) interpretation of the physico-chemical meanings of the apparent kinetic parameters within the universal kinetic description, and (4) extension of the universal kinetic description to encompass the physico-geometrical kinetic modeling.

Introduction of AF, which describes the variation of the reaction rate as a function of $p(H_2O)$ with reference to $P_{eq}(T)$, into the conventional kinetic equation can be a potential approach to describe the kinetics universally as a function of temperature, α, and $p(H_2O)$. Such an AF was derived based on the rate-determining step and steady-state approximations of the elementary steps of the surface nucleation and interfacial reaction processes of the thermal dehydration. An analytical form of AF with the variable exponents (a, b) (eqn (10)) was effectively used to realize the universal kinetic description across different temperatures and $p(H_2O)_{ATM}$ values during the extended Arrhenius-type plot for the IP process (eqn (11)) and the extended Friedman plot for the mass loss process (eqn (13)), where $a = b$ values of 2.70 and 1.20 were optimized for the IP and mass loss processes of the thermal dehydration of SC-MH, respectively. The kinetics of the IP process could be universally described using the extended Arrhenius plot with the AF. Besides, a universal kinetic description for the mass loss process was achieved by successive isoconversional (eqn (13)) and isothermal (eqn (15)) kinetic analyses based on the extended kinetic equation (eqn (12)) with the AF (eqn (10)). For the mass loss process, the universal kinetic description was further refined by considering $p(H_2O)_{EF}$ (eqn (14)), comprising $p(H_2O)_{SG}$ and $p(H_2O)_{ATM}$ with the coefficients (c, d) describing the respective contributions. This approach enabled us to estimate the variation of the contribution of $p(H_2O)_{SG}$ from the changes in the c value as the mass loss process progressed, which indicated the negligible effect at the early stage of the mass loss process, corresponding to the SR process, and the increasing effect at the subsequent stage of the PBR process. On the other hand, the d value remained constant as unity during the reaction. The Arrhenius parameters determined by the extended kinetic approach yielded apparent values due to the simultaneous evaluations of the temperature dependences of the rate constant and $P_{eq}(T)$. Therefore, the intrinsic Arrhenius parameters ($E_{a,int}$, A_{int}) can be estimated by subtracting the contributions of Δ_rH° and Δ_rS° from the respective apparent values (eqn (17) and (18)). All the context of the universal kinetic description *via* the formal kinetic analyses of the extended isoconversional and isothermal kinetic analyses for the mass loss process, as well as the extended Arrhenius-type plot for the IP process, can be applied to the physico-geometrical kinetic modeling based on the IP–SR–PBR model. Consequently, the exponents (a, b), coefficients (c, d), and intrinsic Arrhenius parameters ($E_{a,int}$, A_{int}) were determined for the individual physico-geometrical reaction steps of IP, SR, and PBR, as listed in Tables 1 and 2. The results fulfill the universal kinetic description across different temperatures and $p(H_2O)$ values with physico-chemically meaningful kinetic parameters based on the physico-geometrical kinetic modeling, which were subjected to this study.

The theory and practical procedures of the universal kinetic analysis demonstrated in this study for the thermal dehydration of SC-MH are applicable to the thermal decomposition of other solids that exhibit a reversible nature. The results of each step of the universal kinetic analysis provide specific insights into the kinetics of thermal decomposition across different temperatures and partial pressures of the gaseous product. Furthermore, the kinetic behavior of thermal decomposition at various temperatures and partial pressures of the gaseous product can be simulated using the kinetic parameters determined by the universal kinetic approach, which has the potential to inform the design of the thermal decomposition process for practical applications.

Data availability

Data will be made available on request.

Conflicts of interest

There are no conflicts of interest to declare.

Acknowledgements

The present work was supported by JSPS KAKENHI Grant Numbers 22K02946, 23K22282, 24K05970, and 24K21457.

References

1 H. U. Rammelberg, T. Schmidt and W. Ruck, *Energy Proc.*, 2012, **30**, 362–369.
2 K. E. N'Tsoukpoe, T. Schmidt, H. U. Rammelberg, B. A. Watts and W. K. L. Ruck, *Appl. Energy*, 2014, **124**, 1–16.
3 F. Trausel, A.-J. de Jong and R. Cuypers, *Energy Proc.*, 2014, **48**, 447–452.
4 P. A. J. Donkers, L. C. Sögütoglu, H. P. Huinink, H. R. Fischer and O. C. G. Adan, *Appl. Energy*, 2017, **199**, 45–68.
5 H. U. Rammelberg, T. Osterland, B. Priehs, O. Opel and W. K. L. Ruck, *Sol. Energy*, 2016, **136**, 571–589.
6 Z. Ge, B. Dou, L. Wang, Y. Ding, H. Chen and Y. Xuan, *Carbon Neutrality*, 2022, **1**, 35.
7 X. Yu, Z. Tang, D. Sun, L. Ouyang and M. Zhu, *Prog. Mater. Sci.*, 2017, **88**, 1–48.
8 L. Ouyang, K. Chen, J. Jiang, X.-S. Yang and M. Zhu, *J. Alloys Compd.*, 2020, **829**, 154597.
9 M. R. Usman, *Renewable Sustainable Energy Rev.*, 2022, **167**, 112743.
10 Y. Sun, C. Shen, Q. Lai, W. Liu, D.-W. Wang and K.-F. Aguey-Zinsou, *Energy Storage Mater.*, 2018, **10**, 168–198.
11 Y. Huang, Y. Cheng and J. Zhang, *Ind. Eng. Chem. Res.*, 2021, **60**, 2737–2771.
12 V. Prigiobbe, A. Polettini and R. Baciocchi, *Chem. Eng. J.*, 2009, **148**, 270–278.
13 A. Perejón, L. M. Romeo, Y. Lara, P. Lisbona, A. Martínez and J. M. Valverde, *Appl. Energy*, 2016, **162**, 787–807.
14 F. Raganati and P. Ammendola, *Energy Fuels*, 2023, **37**, 1777–1808.
15 R. Han, Y. Wang, S. Xing, C. Pang, Y. Hao, C. Song and Q. Liu, *Chem. Eng. J.*, 2022, **450**, 137952.
16 F. J. Duran-Olivencia, R. Gannoun, A. T. Perez and J. M. Valverde, *Ind. Eng. Chem. Res.*, 2023, **62**, 1373–1389.
17 D. A. Young, *Decomposition of Solids*, Pergamon, Oxford, 1966.
18 B. Delmon, *Introduction a la Cinetique Heterogene*, Editions Technip, Paris, 1969.
19 A. K. Galwey and M. E. Brown, *Thermal Decomposition of Ionic Solids*, Elsevier, Amsterdam, 1999.
20 C. H. Bamford, C. F. H. Tipper and R. G. Compton, *Reactions of Solids with Gases*, Elsevier, Amsterdam, 1984.
21 J. Szekely, J. W. Evans and H. Y. Sohn, *Gas-Solid Reactions*, Academic Press, New York, 1976.
22 A. K. Galwey, *Thermochim. Acta*, 2000, **355**, 181–238.
23 N. Koga and H. Tanaka, *Thermochim. Acta*, 2002, **388**, 41–61.
24 N. Koga, L. Favergeon and S. Kodani, *Phys. Chem. Chem. Phys.*, 2019, **21**, 11615–11632.
25 M. Fukuda, L. Favergeon and N. Koga, *J. Phys. Chem. C*, 2019, **123**, 20903–20915.
26 S. Kodani, S. Iwasaki, L. Favergeon and N. Koga, *Phys. Chem. Chem. Phys.*, 2020, **22**, 13637–13649.
27 Y. Yamamoto, L. Favergeon and N. Koga, *J. Phys. Chem. C*, 2020, **124**, 11960–11976.
28 J. G. D. Preturlan, L. Vieille, S. Quiligotti and L. Favergeon, *J. Phys. Chem. C*, 2020, **124**, 26352–26367.
29 N. Koga, Y. Sakai, M. Fukuda, D. Hara, Y. Tanaka and L. Favergeon, *J. Phys. Chem. C*, 2021, **125**, 1384–1402.
30 Y. Sakai, S. Iwasaki, S. Kikuchi and N. Koga, *J. Therm. Anal. Calorim.*, 2021, **147**, 5801–5813.
31 Y. Sakai and N. Koga, *Chem. Eng. J.*, 2022, **428**, 131197.
32 M. Hotta, T. Tone, L. Favergeon and N. Koga, *J. Phys. Chem. C*, 2022, **126**, 7880–7895.
33 S. Iwasaki, Y. Zushi and N. Koga, *Phys. Chem. Chem. Phys.*, 2022, **24**, 9492–9508.

34 Y. Zushi, S. Iwasaki and N. Koga, *Phys. Chem. Chem. Phys.*, 2022, **24**, 29827–29840.

35 S. Iwasaki, Y. Sakai, S. Kikuchi and N. Koga, *J. Therm. Anal. Calorim.*, 2022, **147**, 6309–6322.

36 M. Hotta, L. Favergeon and N. Koga, *J. Phys. Chem. C*, 2023, **127**, 13065–13080.

37 M. Hotta, Y. Zushi, S. Iwasaki, S. Fukunaga and N. Koga, *Phys. Chem. Chem. Phys.*, 2023, **25**, 27114–27130.

38 M. Hotta and N. Koga, *Thermochim. Acta*, 2024, **733**, 179699.

39 N. Koga, M. Hotta and L. Favergeon, *J. Phys. Chem. C*, 2024, **128**, 15487–15504.

40 Y. Zushi, S. Iwasaki and N. Koga, *Phys. Chem. Chem. Phys.*, 2022, **24**, 15736–15748.

41 A. C. Baglie and T. C. DeVore, *Thermochim. Acta*, 2022, **717**, 179364.

42 M. C. Ball, C. M. Snelling and A. N. Strachan, *J. Chem. Soc., Faraday Trans. 1*, 1985, **81**, 1761–1766.

43 K. K. Wu and I. D. Brown, *Acta Crystallogr.*, 1975, **31**, 890–892.

44 K. Buijs and C. J. H. Schutte, *Spectrochim. Acta*, 1961, **17**, 917–920.

45 D. D. Wagman, W. H. Evans, V. B. Parker, R. H. Schumm, I. Halow, S. M. Bailey, K. L. Churney and R. L. Nuttall, *The NBS Tables of Chemical Thermodynamic Properties. Selected Values for Inorganic and C1 and C2 Organic Substances in SI Units*, American Chemical Society, Washington, DC, 1982.

46 S. Iwasaki, Y. Zushi and N. Koga, *Phys. Chem. Chem. Phys.*, 2021, **23**, 22972–22983.

47 N. Koga and H. Tanaka, *Thermochim. Acta*, 1994, **240**, 141–151.

48 N. Koga and H. Tanaka, *J. Therm. Anal.*, 1993, **40**, 1173–1179.

49 N. Koga and H. Tanaka, *Thermochim. Acta*, 1992, **209**, 127–134.

50 S. Vyazovkin, K. Chrissafis, M. L. Di Lorenzo, N. Koga, M. Pijolat, B. Roduit, N. Sbirrazzuoli and J. J. Suñol, *Thermochim. Acta*, 2014, **590**, 1–23.

51 W. van Aalst, J. den Holander, W. J. A. M. Peterse and P. M. de Wolff, *Acta Crystallogr.*, 1976, **32**, 47–58.

52 L. D. Hansen, D. J. Eatough, E. A. Lewis, R. G. Bergstrom, D. Degraft-Johnson and K. Cassidy-Thompson, *Can. J. Chem.*, 1990, **68**, 2111–2114.

53 P. Šimon, *J. Therm. Anal. Calorim.*, 2006, **84**, 263–270.

54 N. Koga and T. Kimizu, *J. Am. Ceram. Soc.*, 2008, **91**, 4052–4058.

55 T. Kimura and N. Koga, *J. Phys. Chem. A*, 2011, **115**, 10491–10501.

56 H. Ogasawara and N. Koga, *J. Phys. Chem. A*, 2014, **118**, 2401–2412.

57 M. Fukuda and N. Koga, *J. Phys. Chem. C*, 2018, **122**, 12869–12879.

58 M. Hotta, T. Tone and N. Koga, *J. Phys. Chem. C*, 2021, **125**, 22023–22035.

59 N. Koga, J. Šesták and P. Simon, in *Thermal analysis of Micro, Nano- and Non-Crystalline Materials*, ed. J. Šesták and P. Simon, Springer, Dordrecht, 2013, ch. 1, pp. 1–28, DOI: 10.1007/978-90-481-3150-1_1.

60 S. Vyazovkin, A. K. Burnham, J. M. Criado, L. A. Pérez-Maqueda, C. Popescu and N. Sbirrazzuoli, *Thermochim. Acta*, 2011, **520**, 1–19.

61 H. L. Friedman, *J. Polym. Sci., Part C*, 1964, **6**, 183–195.

62 T. Ozawa, *Bull. Chem. Soc. Jpn.*, 1965, **38**, 1881–1886.

63 T. Ozawa, *Thermochim. Acta*, 1986, **100**, 109–118.

64 J. Málek, *Thermochim. Acta*, 1992, **200**, 257–269.

65 N. Koga, *Thermochim. Acta*, 1995, **258**, 145–159.

66 F. J. Gotor, J. M. Criado, J. Málek and N. Koga, *J. Phys. Chem. A*, 2000, **104**, 10777–10782.

67 J. M. Criado, L. A. Perez-Maqueda, F. J. Gotor, J. Málek and N. Koga, *J. Therm. Anal. Calorim.*, 2003, **72**, 901–906.

68 J. Šesták and G. Berggren, *Thermochim. Acta*, 1971, **3**, 1–12.

69 J. Šesták, *J. Therm. Anal. Calorim.*, 2011, **110**, 5–16.

70 J. Šesták, *J. Therm. Anal.*, 1990, **36**, 1997–2007.

71 N. Koga and H. Tanaka, *J. Therm. Anal.*, 1991, **37**, 347–363.

72 N. Koga and J. Šesták, *Thermochim. Acta*, 1991, **182**, 201–208.

73 N. Koga and J. Šesták, *J. Therm. Anal.*, 1991, **37**, 1103–1108.

74 N. Koga, *Thermochim. Acta*, 1994, **244**, 1–20.

75 A. K. Galwey and M. Mortimer, *Int. J. Chem. Kinet.*, 2006, **38**, 464–473.

76 P. J. Barrie, *Phys. Chem. Chem. Phys.*, 2012, **14**, 318–326.

77 P. J. Barrie, *Phys. Chem. Chem. Phys.*, 2012, **14**, 327–336.

78 D. Xu, M. Chai, Z. Dong, M. M. Rahman, X. Yu and J. Cai, *Bioresour. Technol.*, 2018, **265**, 139–145.

79 A. Mianowski, T. Radko and T. Siudyga, *React. Kinet., Mech. Catal.*, 2020, **132**, 37–58.

80 R. E. Lyon, *J. Phys. Chem. A*, 2023, **127**, 2399–2406.

81 W. D. Spencer and B. Topley, *J. Chem. Soc.*, 1929, 2633–2650, DOI: 10.1039/jr9290002633.

82 K. L. Mampel, *Z. Phys. Chem., Abt. A*, 1940, **187**, 43–57.

83 L. Favergeon, M. Pijolat and M. Soustelle, *Thermochim. Acta*, 2017, **654**, 18–27.